2007-11-13

Shear Modulus Degradation of Liquefying Sand: Quantification and Modeling

Peter A. Olsen
Brigham Young University - Provo

SHEAR MODULUS DEGRADATION OF LIQUEFYING SAND: QUANTIFICATION AND MODELING

by

Peter A. Olsen

A thesis submitted to the faculty of

Brigham Young University

in partial fulfillment of the requirements for the degree of

Master of Science

Department of Civil and Environmental Engineering

Brigham Young University

April 2008

BRIGHAM YOUNG UNIVERSITY

GRADUATE COMMITTEE APPROVAL

of a thesis submitted by

Peter A. Olsen

This thesis has been read by each member of the following graduate committee and by majority vote has been found to be satisfactory.

Date	Travis M. Gerber, Chair
Date	Norman L. Jones
Date	Kyle M. Rollins

BRIGHAM YOUNG UNIVERSITY

As chair of the candidate's graduate committee, I have read the thesis of Peter A. Olsen in its final form and have found that (1) its format, citations, and bibliographical style are consistent and acceptable and fulfill university and department style requirements; (2) its illustrative materials including figures, tables, and charts are in place; and (3) the final manuscript is satisfactory to the graduate committee and is ready for submission to the university library.

Date

Travis M. Gerber
Chair, Graduate Committee

Accepted for the Department

E. James Nelson
Graduate Coordinator

Accepted for the College

Alan R. Parkinson
Dean, Ira A. Fulton College of Engineering and Technology

ABSTRACT

SHEAR MODULUS DEGRADATION OF LIQUEFYING SAND:

QUANTIFICATION AND MODELING

Peter A. Olsen

Department of Civil and Environmental Engineering

Master of Science

A major concern for geotechnical engineers is the ability to predict how a soil will react to large ground motions produced by earthquakes. Of all the different types of soil, liquefiable soils present some of the greatest challenges. The ability to quantify the degradation of a soil's shear modulus as it undergoes liquefaction would help engineers design more reliably and economically.

This thesis uses ground motions recorded by an array of downhole accelerometers on Port Island, Japan, during the 1995 Kobe Earthquake, to quantify the shear modulus of sand as it liquefies. It has been shown that the shear modulus of sand decreases significantly as it liquefies, apparently decreasing in proportion to the increasing excess pore water pressure ratio (R_u). When completely liquefied, the shear modulus of sand (R_u = 1.0) for a relative density of 40 to 50% is approximately 15% of the high-strain modulus of the sand in its non-liquefied state, or 1% of its initial low-strain value.

Presented in this thesis is an approach to modeling the shear modulus degradation of sand as it liquefies. This approach, called the "degrading shear modulus backbone curve method" reasonably predicts the hysteretic shear stress behavior of the liquefied sand. The shear stresses and ground accelerations computed using this method reasonably matches those recorded at the Port Island Downhole Array (PIDA) site. The degrading shear modulus backbone method is recommended as a possible method for conducting ground response analyses at sites with potentially liquefiable soils.

ACKNOWLEDGMENTS

I would like to thank all of my professors that have contributed their time and knowledge to my educational pursuits. I would also like to thank the staff in the Civil Engineering Department office for their patience and support. I must thank Travis M. Gerber for all the time and energy he has contributed during the conversations in his office explaining concepts and principles of engineering. Most of all I need to thank Anne for all of her love and support during these last few years of school.

TABLE OF CONTENTS

LIST OF FIGURES

1 Introduction

1.1 Background

Liquefaction is a general term used to describe a few different types of events that are similar as far as what occurs with respect to soil properties. The devastating effects of liquefaction were dramatically exhibited in 1964. During that year there were two major earthquakes that produced widespread liquefaction, the Good Friday Earthquake in Alaska and the Niigata Earthquake in Japan. Each of these earthquakes produced an enormous amount of damage. Underground structures, bridges, and building foundations were damaged. There were also large settlements in buildings, disrupted roadways, and landslides. Liquefaction contributed in large measure to these failures. Knowledge of liquefaction and its effects have been greatly improved in the last 30 to 40 years, but there is still much to be done in order to protect structures and therefore people from liquefaction damage.

Liquefaction generally occurs in saturated, loose sands. The need for saturation makes liquefaction events occur predominately near rivers, lakes, bays, or other locations where there is a high water table. Pore water pressure builds up during ground shaking due to the tendency for loose sand to compress during shearing. This increase in pore pressure reduces the effective stress in the soil, which is manifest as a reduction in shear strength. This reduction in shear strength often produces some form of failure.

The figures that follow show examples of the types of damage that can result from liquefiable soils. Figure 1-1 shows an example of a liquefaction-induced landslide during the 1964 Alaska earthquake. Once the strength of the soil dropped below the amount needed for static stability, the failure was driven by gravity forces pulling the soil down.

Figure 1-1: Turnagain Heights landslide in Alaska, 1964 (U of W, 2000)

Lateral spreading can occur when a soil liquefies and the combined static and dynamic forces acting on a soil mass exceed the shear strength of the soil. When the combined forces drop below the soil's shear strength, the movement stops. Therefore, lateral spreading is a combination of stop-and-go movement as the dynamic forces fluctuate. This causes gradually sloping soil to move down slope and break into translational blocks. An example of lateral spreading is shown in Figure 1-2. This type

of failure can produce large deformations and is especially dangerous when structures are present.

Figure 1-2: Lateral spreading on Port Island, Japan, 1995 (U of W, 2000)

A sand boil, a feature indicative of liquefaction, is shown in Figure 1-3. Sand boils form as excess pore pressure forces water out of the soil's void space, causing internal erosion and subsequent settlement.

Figure 1-3: Sand boil, Loma Prieta earthquake, 1989 (U of W, 2000)

In order to help mitigate the effects of liquefaction, engineers must be able to quantify the behavior of liquefied soil. In particular, knowing the soil's shear strength under multiple, dynamic loading cycles like those occurring during earthquakes would help engineers predict the resulting ground motions and hence determine appropriate forces to use in the design of structures such as buildings, bridges, embankments, and dams founded on liquefiable soils. Also, engineers would be able to estimate the amount of ground deformations that can occur at such sites.

1.2 Objective of Thesis

The objective of this thesis is two-fold. The first objective is to quantify the degradation of shear strength for sand as it liquefies. The second objective is to develop a simple model which describes how the shear strength of soil (expressed as shear modulus with shear stress versus shear strain) degrades as the soil liquefies. The model is intended to be suitable for predicting soil response and ground motions at a site where there is a potential for liquefaction. These objectives will be fulfilled by using actual earthquake strong motion recordings at the Port Island Downhole Array (PIDA) during the 1995 Kobe (Hyogoken-Nanbu) Earthquake in Japan.

1.3 Organization of Thesis

Chapter 2 will discuss general characterizations of soil behavior and compare a few different methods for predicting earthquake ground motions. Chapter 3 will discuss the nature of the Kobe Port Island Downhole Array (PIDA), followed by a review of two previous studies of liquefied soil done using PIDA data. In Chapter 4, a method for calculating the shear stresses and shear strains for a soil layer from measured acceleration

time histories is presented. Also presented in Chapter 4 are shear stress-strain time histories and hysteric loops for liquefying sand computed from PIDA data. Chapter 5 presents a modeling method which quantifies the shear modulus degradation for liquefying sand. Chapter 6 will summarize the results of this thesis, present conclusions, and provide recommendations for future research regarding the shear stress-strain behavior of liquefied soil.

2 Review of Concepts and Analytical Methods

2.1 Characterization of Soil Behavior

To define or quantify the degradation of the strength of soil in response to shearing, a maximum shear modulus value and a shear modulus degradation curve are commonly used. The slope of the shear stress versus shear strain plot is the shear modulus. Therefore, shear modulus is defined as shear stress divided by shear strain. Since soil response to shearing is non-linear, the shear modulus varies with the level of strain.

A shear stress versus shear strain plot for a soil during an earthquake may contain many hysteretic loops. Along each loop there are a few different ways to define the shear modulus. One definition is the tangent shear modulus. The tangent shear modulus is the slope of the loop at any point in time or the change in stress divided by the change in strain for a very small time increment. Another method of defining the shear modulus is to use the secant shear modulus. The secant shear modulus can be calculated at any point in time by dividing the total stress by the total strain. It is common to simplify secant shear moduli by defining one equivalent shear modulus for a single hysteretic loop. The equivalent shear modulus is determined by connecting the extreme (high and low) shear stresses and shear strains on the loop with a single line and calculating its slope. This equivalent shear modulus value is commonly represented by the symbol "*G*".

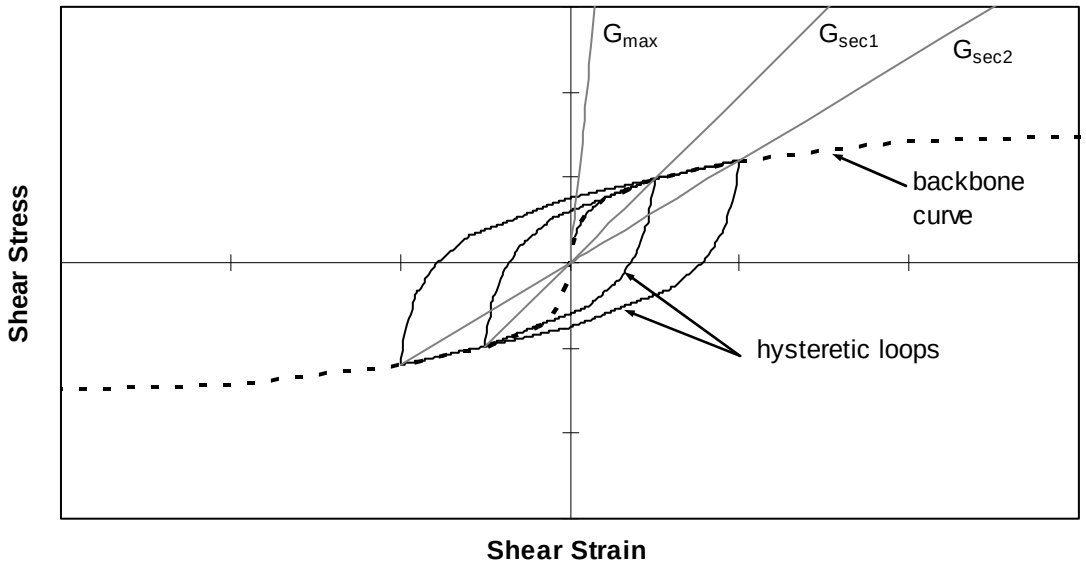

Figure 2-1: Illustration of shear modulus on a plot of shear stress vs. shear strain

Figure 2-1 illustrates the difference between the initial or maximum tangent shear modulus, G_{max}, and secant shear moduli, G_{sec1} or G_{sec2} (or simply G), as subsequent hysteretic loops are formed. The maximum (low-strain) shear modulus for a soil is often determined using the soil's shear wave velocity as shown in Equation 1:

$$G_{\max} = \rho V_s^2 \tag{2.1}$$

where ρ is the mass-density of the soil and V_s is the shear wave velocity of the soil. The backbone curve shown in Figure 2-1 is the shear stress-strain response under a monotonic (non-cyclic) loading. Soil backbone curves commonly become asymptotic at larger strains, indicative of plastic deformation and failure.

A shear modulus degradation curve (also referred to as a G/G_o or G/G_{max} curve) is a more direct method for showing how secant shear moduli vary with shear strain. In a shear modulus degradation curve, secant shear moduli are normalized (or divided) by the

initial or maximum shear modulus. The general shape of a shear modulus degradation curve is shown in Figure 2-2 (note the logarithmic abscissa). This normalized shear modulus curve allows soils with different maximum moduli to be compared. The curve shown in Figure 2-2 was created by Seed and Idriss (1970) and represents the "average" degradation of shear modulus with respect to cyclic shear strain for sands.

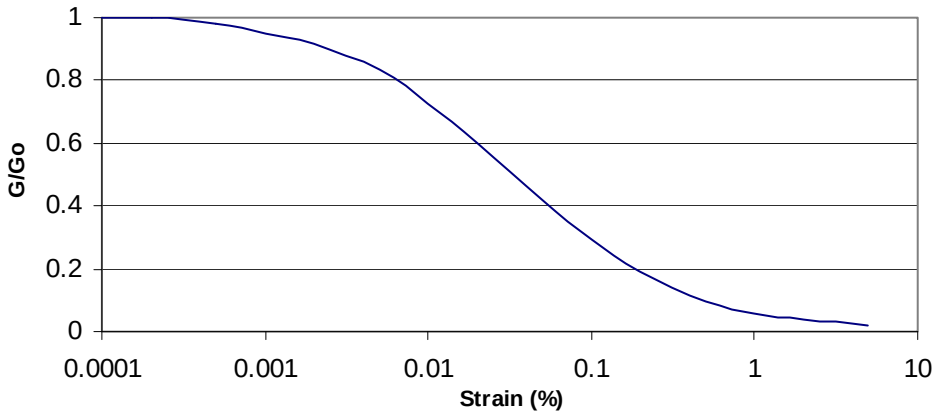

Figure 2-2: Average shear modulus degradation curve for sand (Seed & Idriss, 1970)

Energy dissipation in the soil can be accounted for by using a damping ratio. While damping can be found directly using the area enclosed by hysteretic loops, it is sometimes helpful (particularly when using the equivalent linear approach with a shear modulus degradation curve) to describe damping as a separate function. The damping ratio is a function of the plasticity of the soil and shear strain, among other parameters. The damping ratio is never zero, although it is very small at low strains. As strain increases, the damping ratio also increases. Seed and Idriss' "average" damping curve for sand corresponding to the modulus degradation curve shown in Figure 2-2 is presented in Figure 2-3.

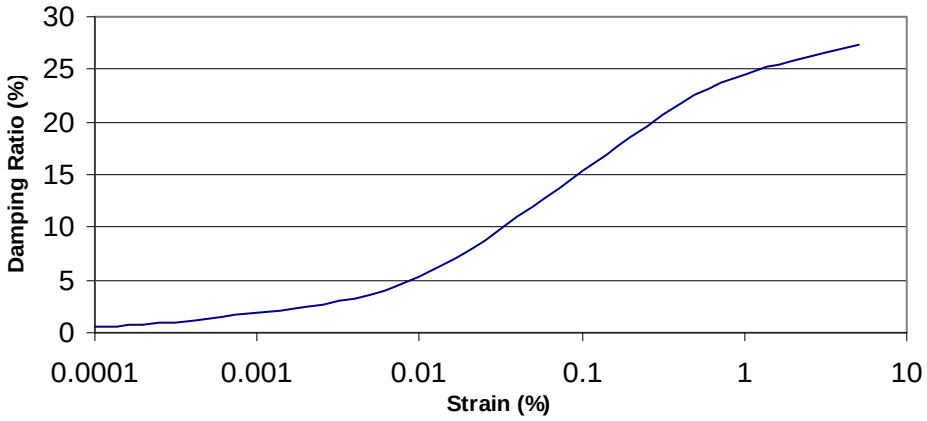

Figure 2-3: Average damping ratio curve for sand (Seed & Idriss, 1970)

2.2 Prediction of Earthquake Ground Motions

There are a variety of methods that can be used to analyze or predict the response of sites to earthquake ground motions. These methods can be grouped into three general groups. One method is known as the equivalent linear method (ELM). A computer program using the equivalent linear method is SHAKE, developed by Schnabel et al. (1972). Another method for earthquake analysis is the non-linear method (NLM). One computer program using this type of analysis is NERA (Nonlinear Earthquake site Response Analysis of layered soil deposits), encoded by Bardet and Tobita (2001). The primary analytical method used in this thesis for analyzing time histories and modeling shear modulus degradation is an adaptation of the NERA program methodology. Finite element/difference analyses are the third type of method used for earthquake analysis. This method of analysis is beyond the scope of this paper and will not be discussed. Both SHAKE and NERA require that the individual soil strata be characterized as homogenous and isotropic. Both methods are also one-dimensional, analyzing only vertically propagating shear waves.

2.2.1 Equivalent Linear Method (ELM)

The equivalent linear method uses a single shear modulus value to represent a soil's stress-strain response throughout the entire period the soil is subjected to ground shaking. Instead of following a non-linear stress-strain backbone curve in response to changes in strain, the shear stress-strain relationship is defined by the secant shear modulus line. These two different curves are illustrated in Figure 2-4. There is no hysteretic behavior in the ELM; therefore, damping must be defined as its own function. An iterative approach is commonly used in the ELM to find a shear modulus value on the shear modulus degradation curve that is compatible with the shear strains produced by propagating waves.

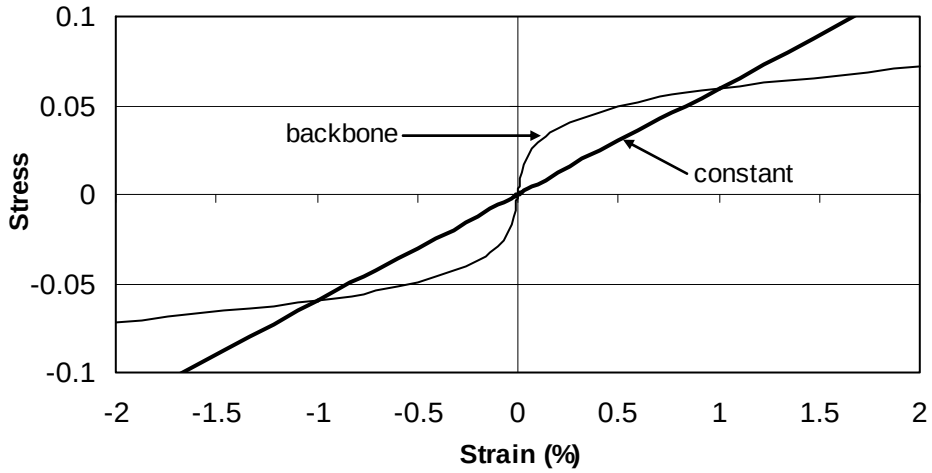

Figure 2-4: Backbone and equivalent shear modulus curve

2.2.1.1 SHAKE Computer Program

The ELM has been incorporated into the computer program SHAKE (Schnabel et al, 1972). Work on this thesis used a more modern code, PROSHAKE, developed by

EduPro Civil Systems (1998). The following is a basic outline of steps performed in conducting a SHAKE/PROSHAKE analysis (Schnabel et. al., 1972):

1. Acquire the time history of the input or base motion. This can be displacement, velocity, or acceleration. Assign this motion to a layer within the subsurface profile.
2. Next, the motion needs to be converted into the frequency domain and expressed as a Fourier series. This information consists of the amplitude of the waves that constitute the earthquake motion expressed in the frequency domain.
3. A transfer function between two layers is found using the concept that the amplitude of stress, strain, and displacement has to be equal at the boundary of the two layers. The transfer function is also expressed in the frequency domain; hence, each frequency has its own multiplier. Parameters such as the complex shear modulus, the complex wave number, and the complex impedence ratio (where 'complex' refers to values having both real and imaginary parts) are needed to define the transfer function. These parameters in turn depend on the known properties of each soil layer: thickness, mass density, shear modulus, and damping ratio. The formulation of a specific transfer function depends on the boundary conditions presented by the layer in which the ground motion is known (usually the bottom-most layer which is bedrock) as well as the properties of all of the other layers; hence, a recursion process is used which solves for the amplitude coefficients of the wave equation within each layer.
4. After using the transfer function to determine the frequency based motions within the layer(s) of interest, the last step of the process is to convert the Fourier series

from the frequency domain back to the time domain. This conversion inherently assumes soil linearity and that the principle of superposition is applicable.

After these steps have been completed, values such as acceleration, velocity, and displacement are explicitly known for the entire time history, and values such as stress and strain are readily determined.

In the PROSHAKE input motion interface, a few parameters such as strain ratio, maximum number of iterations, and error tolerance are specified. The strain ratio is a number (usually 0.65 for a 7.5 magnitude earthquake) used to account for the fact that the laboratory loading conditions used to produce shear modulus degradation curves are more severe than the actual loadings produced by an earthquake. The strain ratio is multiplied by the maximum shear strain value in the shear strain time history, and the resulting shear strain and corresponding shear modulus to be used in solving the seismic wave equations are plotted on the same plot as the shear modulus degradation curve. If the point does not correspond to the curve within the error tolerance specified, than the shear modulus is adjusted and the process repeated. The new values are compared once again to the modulus curve. The shear modulus value is iterated until the point is within the error tolerance or the maximum number of iterations occurs.

There are a number of shortcomings in the ELM when dealing with liquefied soils. Primarily, soil does not act in a linear fashion, and therefore, the ELM is approximating the non-linear stress-strain relationship with a linear relationship. This linear relationship also means that the method assumes that the shear modulus is constant throughout the duration of the ground motion. In actuality, the shear modulus value is constantly changing (particularly as the soil undergoes the liquefaction process)

throughout the duration of the ground motion. While this shortcoming is true when using the ELM with most soils, its consequences are even more pronounced in liquefied soils, where the loss of shear strength is large and the full range of shear modulus values cannot be reasonably approximated with a single "average" value.

2.2.2 Nonlinear Method (NLM)

The nonlinear analysis differs from the equivalent linear method in that the shear modulus value is not constant. Instead of using a strain ratio and iterating to find a single constant shear modulus value to use for the entire time history of ground motion, the shear modulus is constantly adjusted in response to changes in strain.

The stress-strain backbone curve remains the same curve used in the equivalent linear analysis. The shear stress-strain relationship traces the backbone curve until the first stress reversal occurs. This initial curve and the remaining hysteretic loops are formed using Masing rules. There are four basic rules comprised in the Masing rules as follows (Kramer, 1996):

1. For the initial loading, the stress-strain curve follows the backbone curve.
2. The unloading and reloading curves have the same shape as the backbone curve. The origin is shifted to the point of stress reversal and the backbone curve is doubled.
3. If the strain value for the previous stress reversal is exceeded than the unloading or reloading curve intersects and follows the backbone curve until the next stress.
4. If an unloading or reloading curve crosses another curve from a previous cycle then the curve will follow that previous unloading or reloading curve.

This method allows the shear stress-strain relationship to be nonlinear. The nonlinearity of the relationship is defined by the prescribed backbone curve and the Masing rules. The backbone curve itself is constant and does not degrade in this nonlinear analysis.

2.2.2.1 Nonlinear Earthquake Site Response Analysis of Layered Soil Deposits (NERA) Computer Program

NERA is a computer program that utilizes FORTRAN 90 and Excel Visual Basic programming to implement the NLM. NERA uses an Iwan-Mroz (IM) model consisting of a set of sliding springs of varying stiffness to model hysteretic stress-strain behavior according to Masing rules. The parameters of the IM model are defined so that the model replicates shear modulus degradation curves typically used in the ELM. NERA uses a finite difference formulation to solve wave propagation equations in the time domain.

The data required for each layer of soil in the NERA procedure is similar to that needed for the ELM in PROSHAKE and consists of layer thickness, density, initial shear modulus, and a description of how shear modulus varies with shear strain. Additionally, a time history of acceleration is typically needed to describe the motion of the underlying bedrock or bottom layer of the system. Figure 2-5 is a schematic which shows the notation used in the NERA model to identify the various soil layers at whose boundaries nodes are placed and acceleration, velocity, and displacement are computed. Additional nodes are typically placed at the center of each layer at which points shear stresses and strains are computed. The algorithm in NERA assumes a constant level of shear stress and strain throughout each layer.

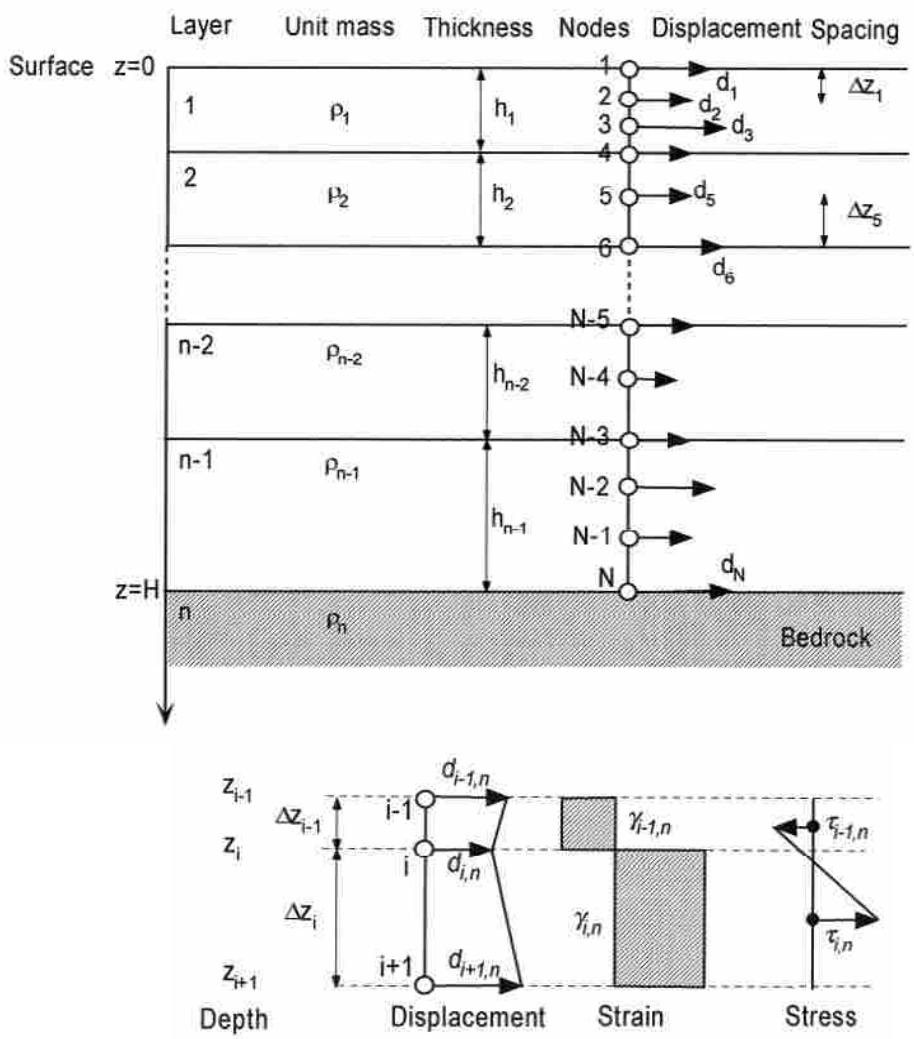

Figure 2-5: Schematic of a layered soil profile and two individual layers showing the notation used in the NERA algorithm (Bardet and Tobita, 2001)

In the discussion and equations which follow, the subscript "I" is associated with the input motion at the base or bedrock level, the subscript "i" represents the soil node or layer with the number 1 representing the uppermost node or layer, and the subscript "n" represents the respective time step. When performing a ground response analysis with the NERA algorithm, the initial values (at time step n=1) for displacement, predicted velocity, and acceleration are set to zero for all layers, and the shear stress and shear strain for all layers are set to zero for n=0. The prescribed acceleration and input velocity

are also equal to zero for n=0. Next, the shear strain, shear strain increment, and shear stress are calculated at each node / layer for the subsequent time step (which is n=1 for the first iteration). Equation 2.2 is used to calculate the strain.

$$\gamma_{i,n} = \frac{d_{i+1,n} - d_{i,n}}{\Delta z_i} \tag{2.2}$$

where d is the displacement, Δz is the layer thickness, and γ is the shear strain at the respective layer and time step increment. The determination of displacement is discussed later. The strain increment is calculated by taking the difference of the strain from the current time step and the strain from the previous time step. The stress is found by using the Iwan-Mroz (IM) model with the stress from the previous time step and strain increment as the inputs. The shear stress calculated using the IM model is consistent with a user-defined shear modulus degradation backbone curve with hysteretic behavior defined by the Masing rules.

The third step in the algorithm is to calculate the input velocity by using Equation 2.3 to integrate the input acceleration.

$$V_{I,n} = V_{I,n-1} + \frac{1}{2}(a_{I,n} + a_{I,n-1})\Delta t \tag{2.3}$$

where $V_{I,n}$ is the input velocity, $V_{I,n-1}$ is the input velocity for the previous time step, $a_{I,n}$ is the input acceleration, $a_{I,n-1}$ is the input acceleration from the previous time step, and Δt is the time step increment or interval of the time history.

The next step is an implementation of a Newmark-based central difference formula in which a "predicted" velocity is calculated. There are three separate

formulations for the predicted velocity based on boundary conditions (one for the bottom layer, one for the top layer, and one for layers in-between). These three equations are shown as Equations 2.4, 2.5, and 2.6, respectively.

$$\widetilde{v}_{N,n+1} = \frac{\widetilde{v}_{N,n}(\Delta z_{N-1} - v_s \Delta t) + 4 v_s V_{I,n} \Delta t - 2\tau_{N-1,n} \Big/ \rho_b}{\Delta z_{N-1} + v_s \Delta t} \tag{2.4}$$

$$\widetilde{v}_{1,n+1} = \widetilde{v}_{1,n} + \left(\frac{2\tau_{1,n}}{\Delta z_1}\right)\left(\frac{\Delta t}{\rho_1}\right) \tag{2.5}$$

$$\widetilde{v}_{i,n+1} = \widetilde{v}_{i,n} + 2\left(\frac{\tau_{i,n} - \tau_{i-1,n}}{\Delta z_i + \Delta z_{i-1}}\right)\left(\frac{\Delta t}{\rho_i}\right) \tag{2.6}$$

where $\tilde{v}$ is the predicted nodal velocity for the respective node and time step, τ is the shear stress for the respective layer and time step, ρ_i is the unit density of layer i, Δz is the thickness of the specified layer, v_s is the shear wave velocity of the specified layer, and Δt is the time step increment or interval.

After computing the predicted velocity, the final step in the NERA algorithm is to use the predicted velocity to calculate the displacement, velocity and acceleration. The equation for each of these values is shown in Equations 2.7, 2.8, and 2.9.

$$d_{i,n+1} = d_{i,n} + \widetilde{v}_{i,n+1} \Delta t \tag{2.7}$$

$$v_{i,n} = \frac{1}{2}(\widetilde{v}_{i,n+1} + \widetilde{v}_{i,n}) \tag{2.8}$$

$$a_{i,n} = \frac{1}{\Delta t}(\tilde{v}_{i,n+1} - \tilde{v}_{i,n}) \quad \textbf{(2.9)}$$

where *d* is the displacement, *v* is the velocity, and a is the acceleration for the respective node and time step. This process is repeated for each time step to determine the entire time history of displacement, velocity, acceleration, shear stress, and shear strain for each node / layer within the soil profile.

A shortcoming of the NERA procedure and the NLM in general is that the process has not been widely adopted by the professional engineering community. The required inputs for PROSHAKE and NERA are similar, and the level of accuracy appears to be generally comparable, but in favor of NERA. Perhaps the lack of widespread use of the NLM stems from unfamiliarity and inexperience among practitioners and the greater computational resources required (which is really no longer an issue with the evolution of computer capacity).

3 Data and Studies of the Port Island Downhole Array

3.1 1995 Kobe, Japan, Earthquake

At 5:46 AM (local time) on January 17, 1995, the Hyogoken-Nanbu (Japan) Earthquake occurred. The magnitude 6.9 (M_j = 7.2) earthquake is referred to as "the Great Hanshin Earthquake Disaster." The epicenter of the earthquake was located just north of Awaji Island, at a relatively shallow depth of 13.3 km. The damage caused by this earthquake was enormous with over 5,500 people killed, 37,000 injured, and extensive damage (USGS, 2006). The larger portion of these deaths was caused by roofs falling on top of the persons and then being burned by fire following the earthquake. The number of separate fires reported was 164, a large portion starting within 24 hours after the earthquake. The total dollar amount of damage was estimated to be 96.3 billion U.S. dollars.

3.2 Port Island

Port Island is a man-made island which serves as a major port facility located to the southwest of Kobe, Japan. The configuration of a portion of the island is shown in Figure 3-1. During the period from 1966 to 1981, a 436-ha area was reclaimed by bottom dumping fill material from barges. The second phase of the island was built towards the south from 1986 to 1996. The depth of the first phase reclaimed area is 19 meters with 4 meters above sea level. There were few areas of the island that received soil treatment

other than compaction on the reclaimed portion above the water table. Consequently, there was a significant risk of liquefaction due to the use of a granular soil placed with low compaction effort in a saturated environment. During the Kobe Earthquake, widespread liquefaction occurred on Port Island. There was a maximum settlement of 3 meters, with 0.5 to 1 meter average settlement over the whole island (Elgamal et. al., 1996).

3.3 Port Island Downhole Array (PIDA)

In 1991, an array of triaxial accelerometers was installed in the northwest portion of the island. This array of accelerometers is referred to as the Port Island Downhole Array (PIDA). The location of PIDA on the island can be seen in Figure 3-1. The accelerometers in the array are located at the ground surface and depths of 16, 32, and 83 m as shown in Figure 3-2.

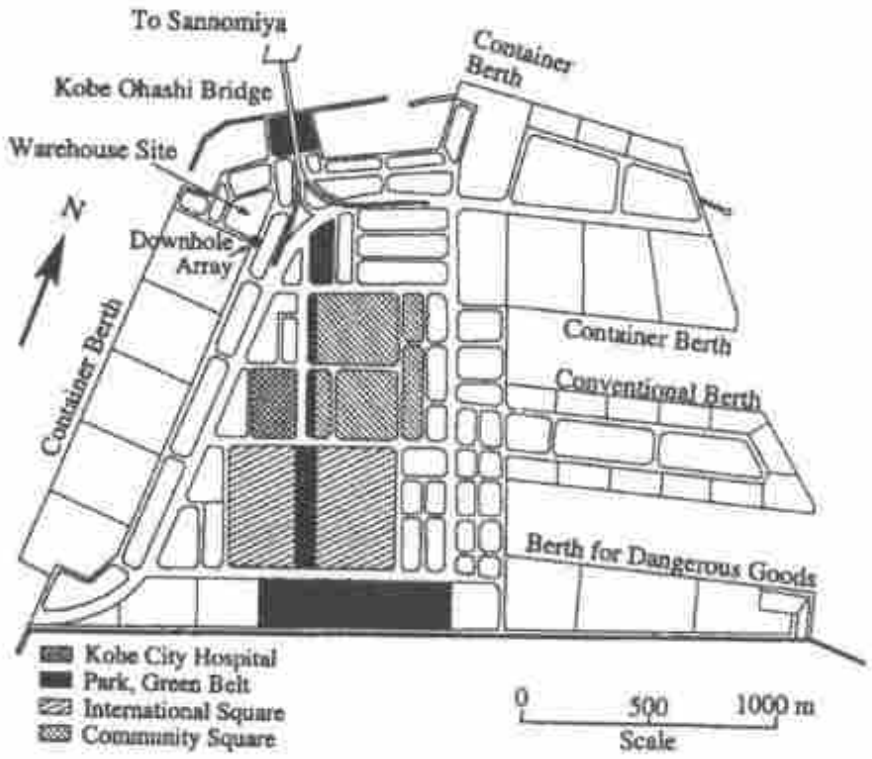

Figure 3-1: PIDA location on Port Island (Nakakita and Watanabe, 1981)

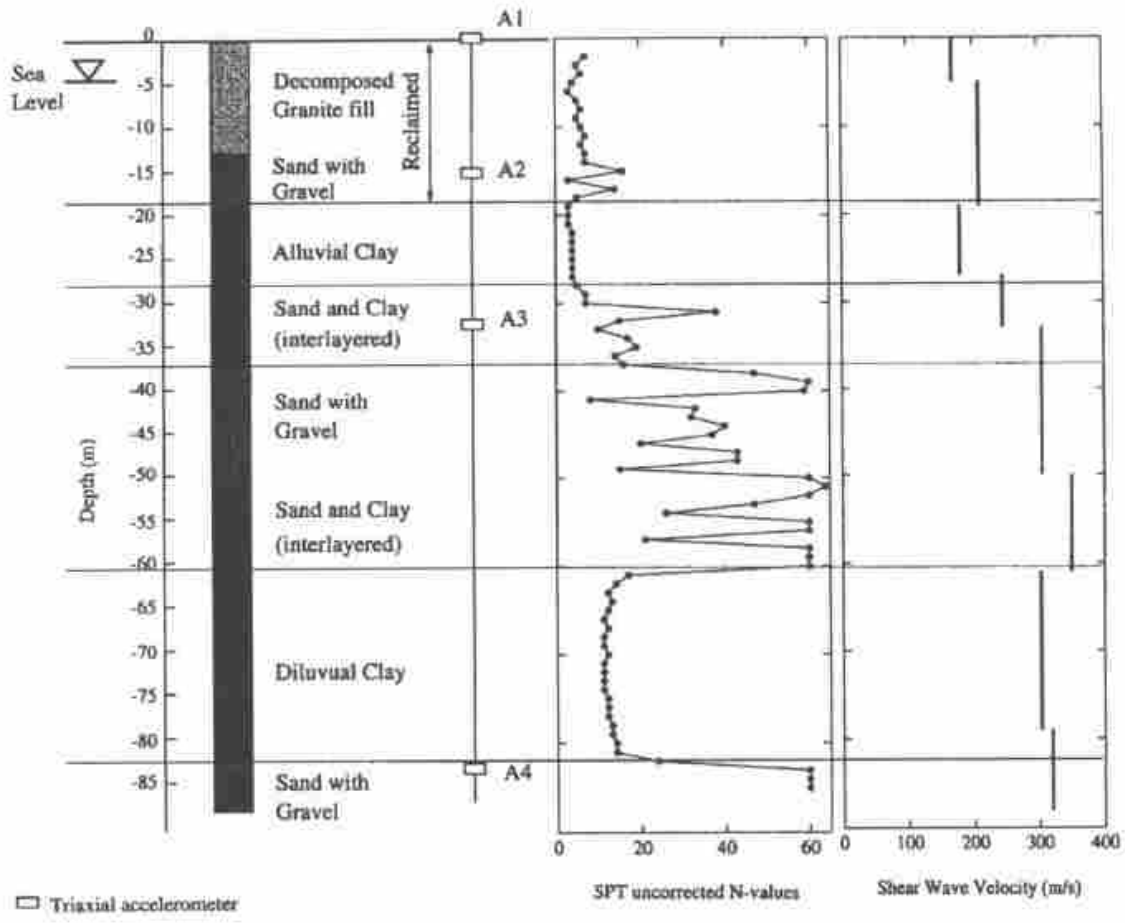

Figure 3-2: PIDA soil profile on Port Island (Elgamal et al, 1996)

Also shown in Figure 3-2 are the subsurface conditions for the PIDA site. The initial 19 m of soil is reclaimed fill consisting of 13 m of decomposed granite fill (locally referred to as "masado") overlying a mixture of sand and gravel. Underneath the reclaimed fill is 8-m of soft, very plastic alluvial clay, followed by layers of sand and stiffer clay. Uncorrected standard penetration test (SPT) blow counts in the reclaimed material average about 6, indicating a low relative density. A comparably low shear wave velocity of 210 m/sec was also measured for this material. While gradation of the

material varies, the mean grain size of the particles is on the order of 2 mm. (Ishihara et al., 1998)

During the 1995 Kobe earthquake ground motions were recorded at the PIDA site. Acceleration time histories recorded during the initial earthquake for the North-South direction are presented in Figure 3-3 through Figure 3-5. It is interesting to note that the maximum acceleration for the 16 m and 32 m depths is approximately 0.55 g, while the maximum acceleration at the ground surface is approximately 0.3 g. The lower maximum acceleration is attributable to soil softening that apparently occurs once the acceleration at the 16 m depth exceeds 0.1 g at about 7.4 sec, and has definitely occurred by the time of the arrival of the first 0.3 g pulse at about 8 sec.

The velocities for the North-South direction are presented in Figure 3-6 through Figure 3-8. The same soil softening seen in the acceleration time histories is shown by the velocity initially being amplified as the seismic waves reach the surface. But after the maximum acceleration occurs in the surface layer at about 9 sec, the rest of the velocity time history in Figure 3-6 is de-amplified relative to the lower layer velocities. There is not much change in the 32 m velocities compared to the 16 m velocities except for a little magnification of the amplitude.

The displacement time histories for the North-South direction are presented in Figure 3-9 through Figure 3-11. The same relationships present in the velocity time histories are also present in the displacement time histories. Some of the smaller relative maximum and minimum oscillations found in the 16 and 32 m depth time histories after 10 sec are damped out in the surface time history. The amplitude of the larger maximum and minimum displacements is still slightly larger than those in the 16 m time history.

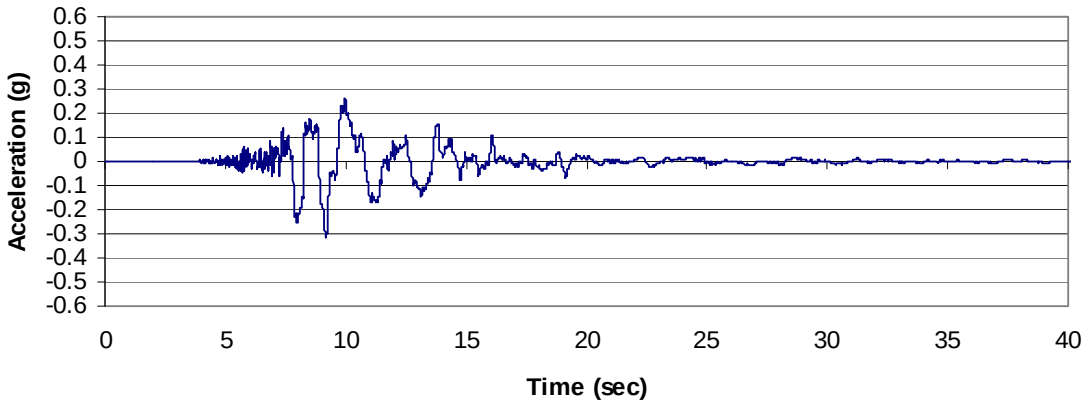

Figure 3-3: NS surface time history of acceleration at PIDA

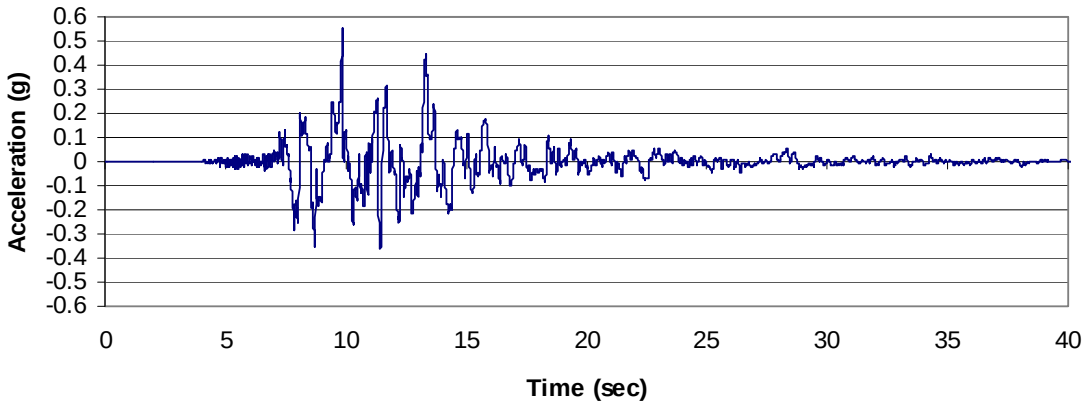

Figure 3-4: NS 16 meter time history of acceleration at PIDA

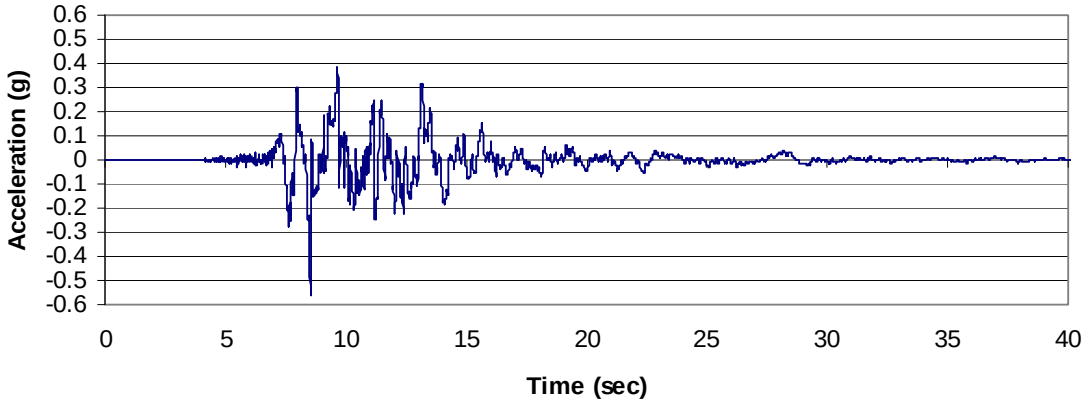

Figure 3-5: NS 32 meter time history of acceleration at PIDA

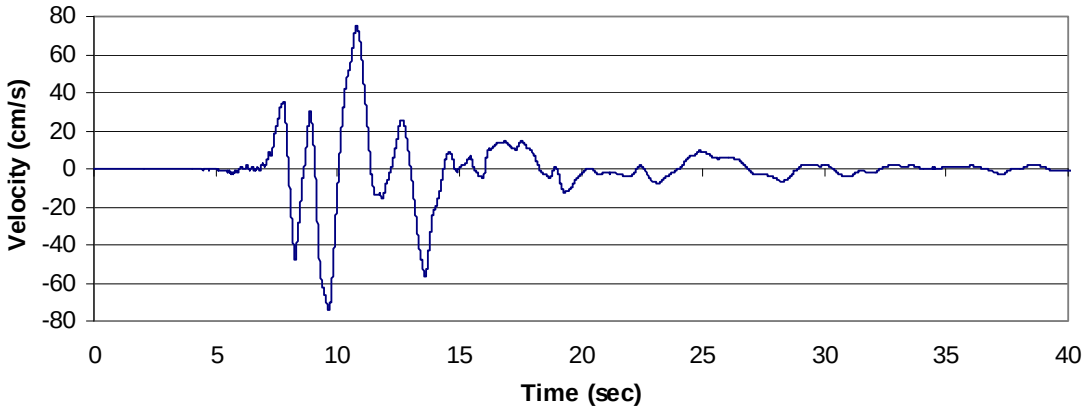

Figure 3-6: NS surface time history of velocity at PIDA

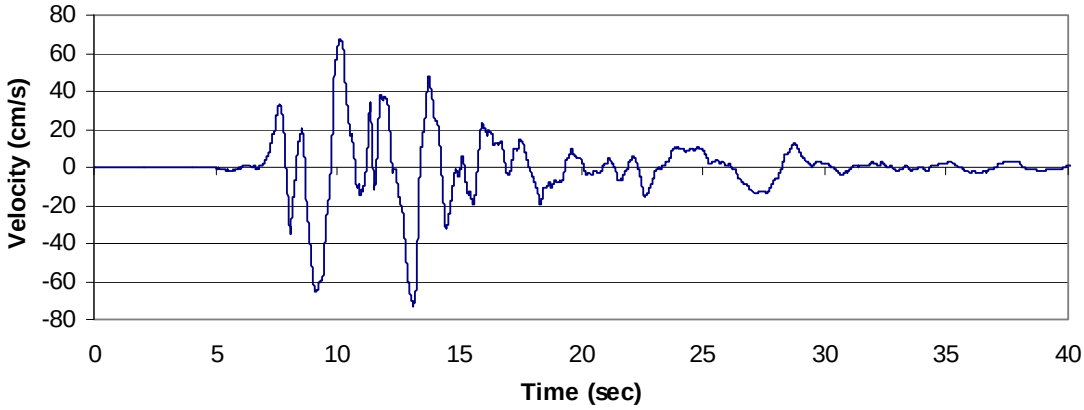

Figure 3-7: NS 16 meter time history of velocity at PIDA

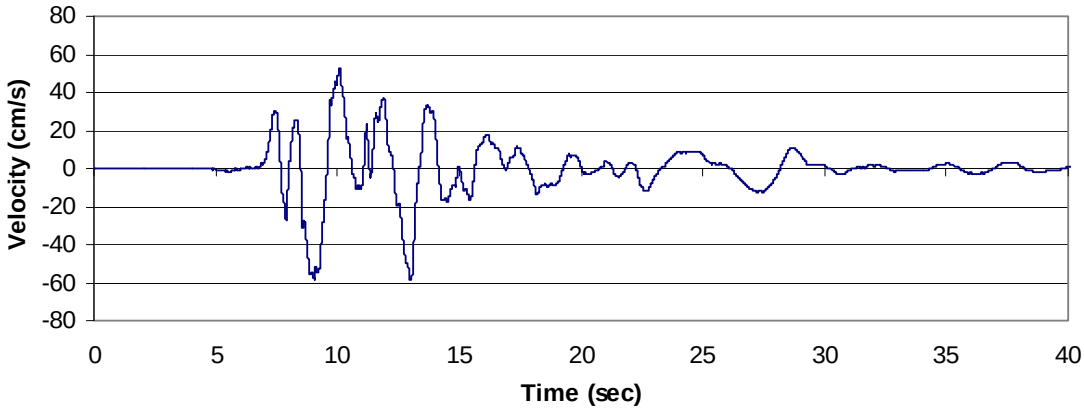

Figure 3-8: NS 32 meter time history of velocity at PIDA

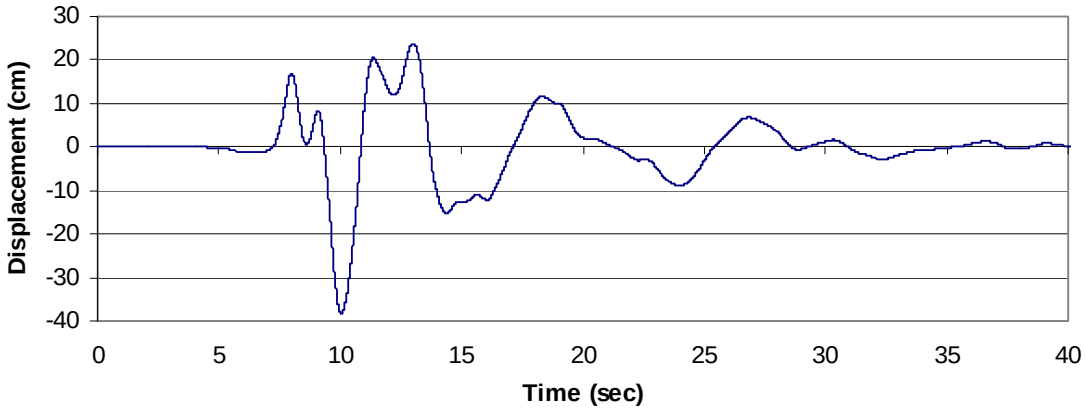

Figure 3-9: NS surface time history of displacement at PIDA

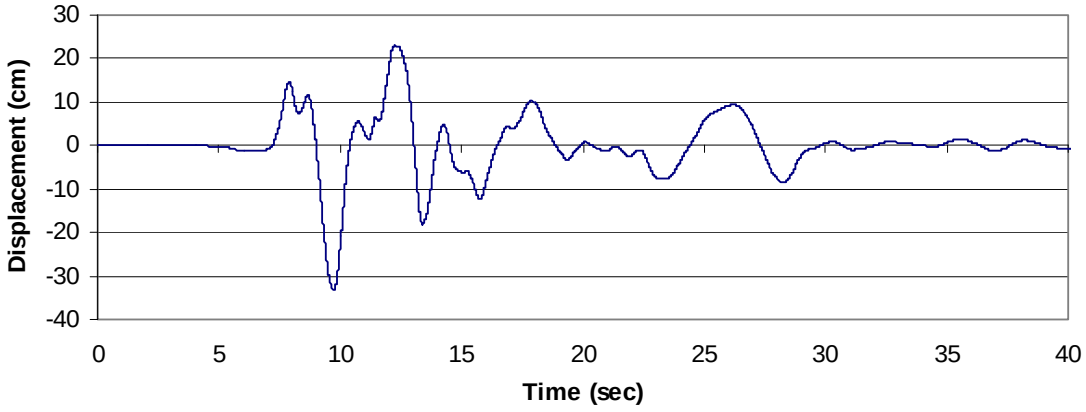

Figure 3-10: NS 16 meter time history of displacement at PIDA

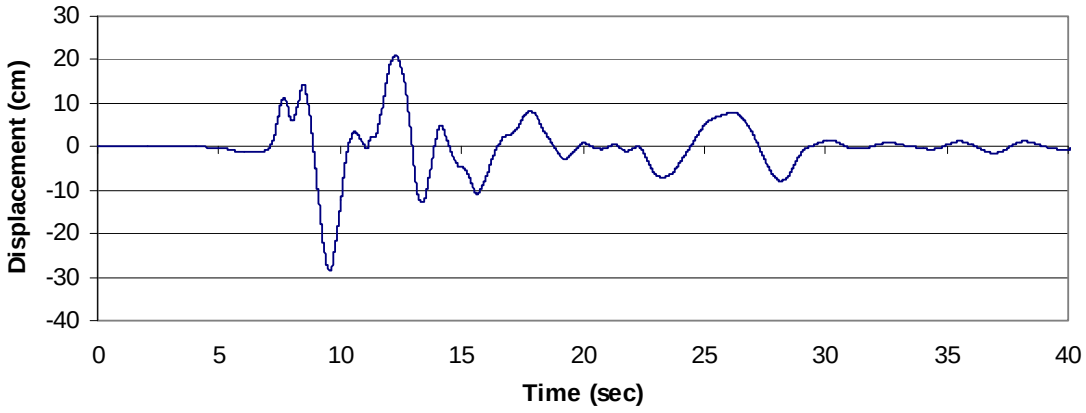

Figure 3-11: NS 32 meter time history of displacement at PIDA

The acceleration time histories for the East-West direction are presented in Figure 3-12 through Figure 3-14. The time histories for velocity in the East-West direction are presented in Figure 3-15 through Figure 3-17. The time histories for displacement in the East-West direction are presented in Figure 3-18 through Figure 3-20. The observations made for the North-South motions also apply to the East-West motions.

The acceleration response spectra for the three depths also show some interesting behaviors. Figure 3-21 through Figure 3-23 present the acceleration response spectra for the 0, 16, and 32 m depths in the North-South direction. Each response spectrum contains five different curves. The uppermost curve shows the "full" spectrum based on the entire time history. The other four curves are response spectra based on truncated time histories at the selected points in time.

The effects of liquefaction within the 0 to 16 m layer of fill can be seen when the three figures are compared. Figure 3-21 shows the peak spectral acceleration occurring at a period of approximately 1.3 seconds. At the 16 and 32 m depths, peak spectral accelerations occur at much lower periods. Additionally, the peak spectral acceleration at the 16 m depth is 1.4 g whereas the peak spectral acceleration of the surface layer is slightly above 1.0 g. The lower peak acceleration and the higher period associated with the peak acceleration of the surface layer indicates significant soil softening within the soils located between 0 and 16 m.

Figure 3-24 through Figure 3-26 present acceleration response spectra for all accelerometer depths in the East-West direction. The East-West direction acceleration response spectra are similar to those of the North-South direction, with the main difference being that the behavior is not nearly as pronounced.

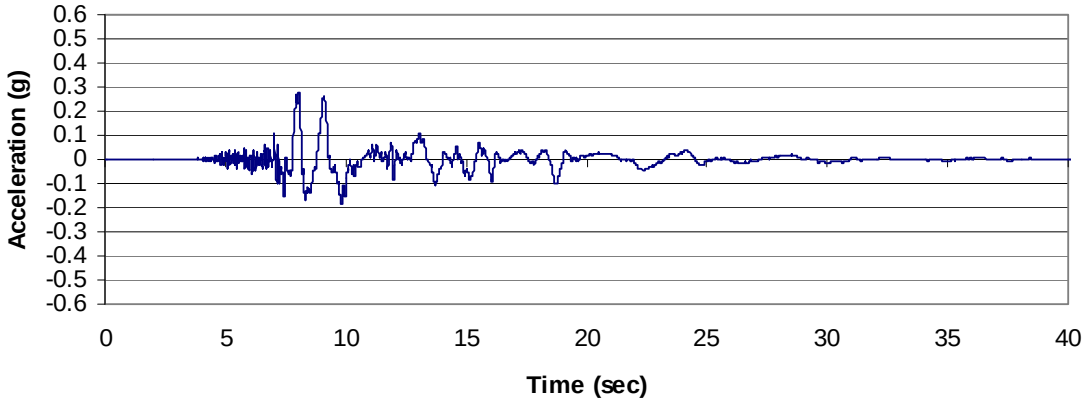

Figure 3-12: EW surface time history of acceleration at PIDA

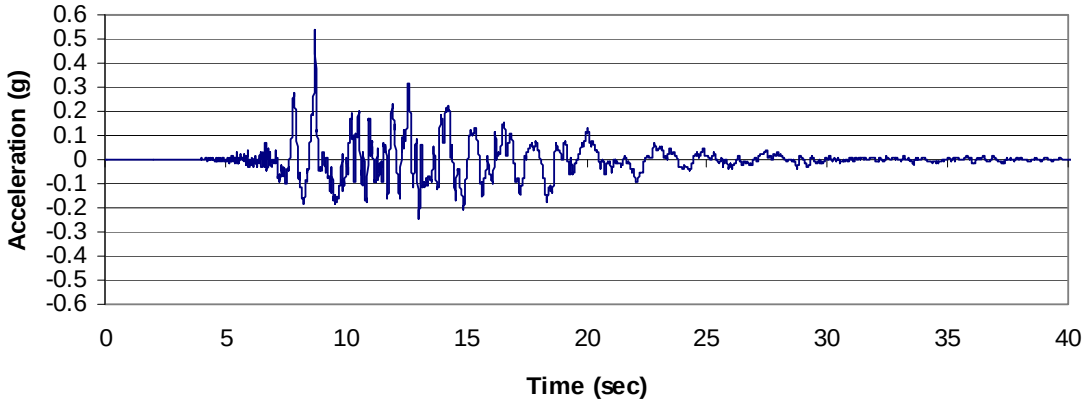

Figure 3-13: EW 16 meter time history of acceleration at PIDA

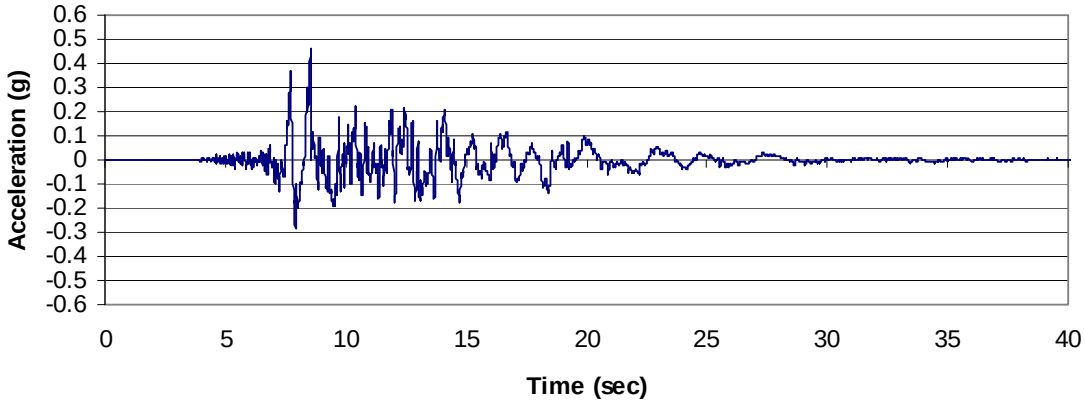

Figure 3-14: EW 32 meter time history of acceleration at PIDA

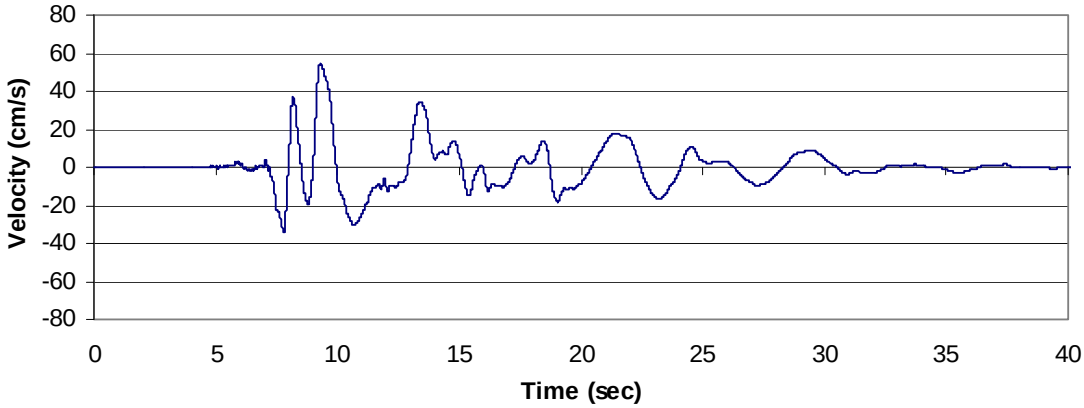

Figure 3-15: EW surface time history of velocity at PIDA

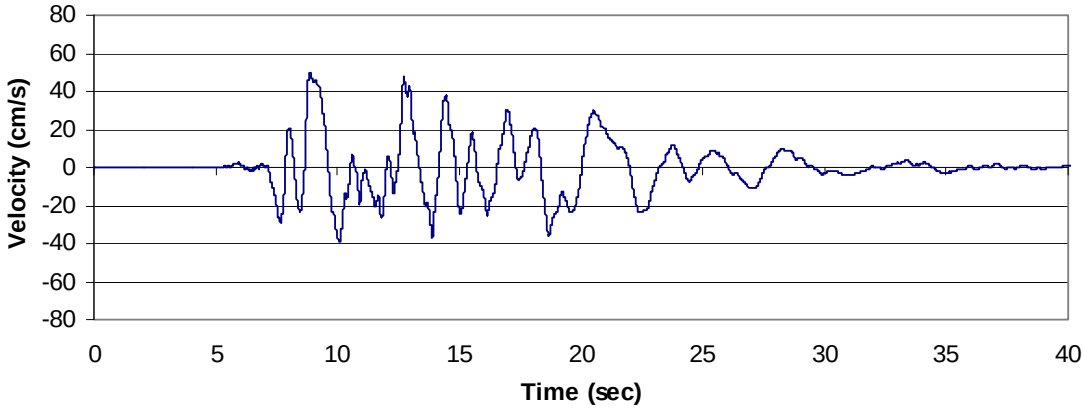

Figure 3-16: EW 16 meter time history of velocity at PIDA

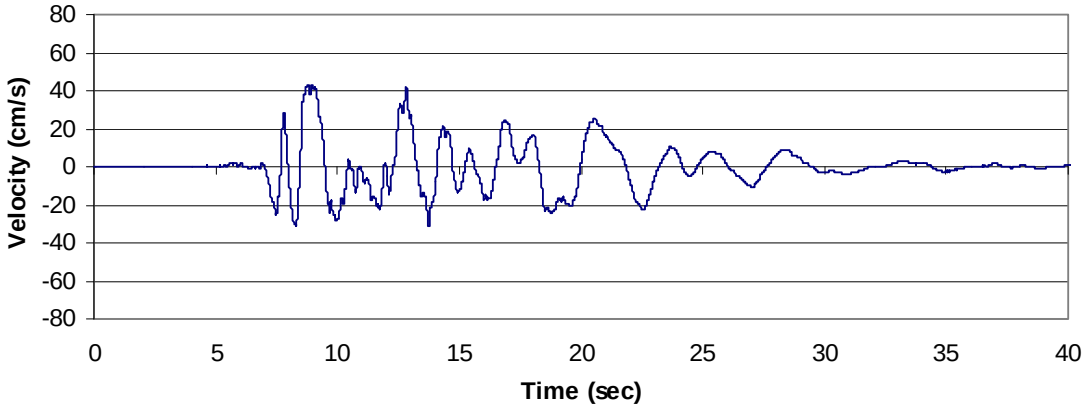

Figure 3-17: EW 32 meter time history of velocity at PIDA

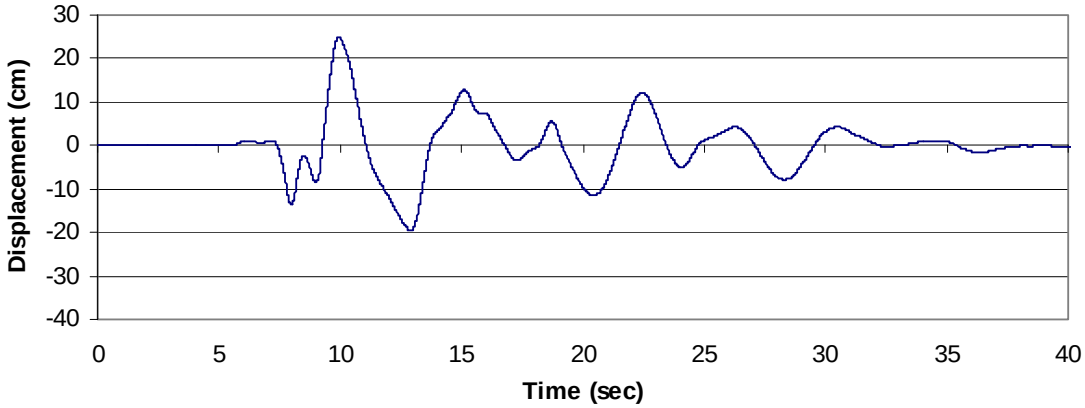

Figure 3-18: EW surface time history of displacement at PIDA

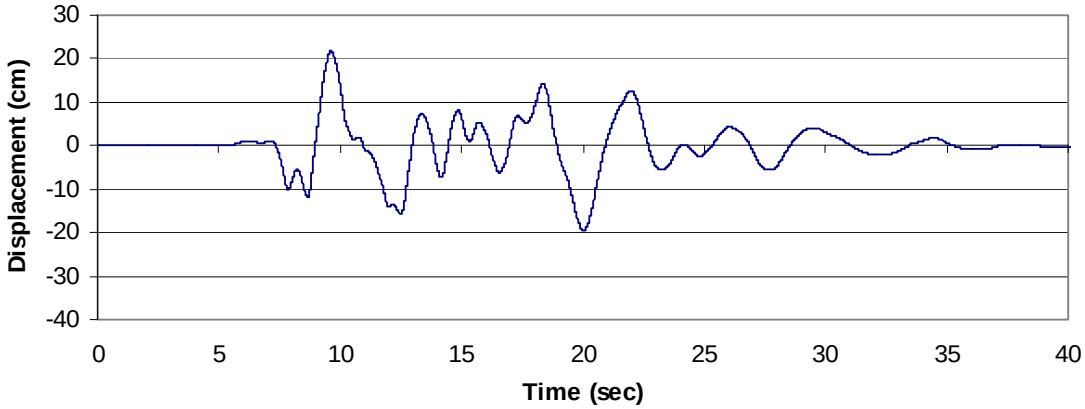

Figure 3-19: EW 16 meter time history of displacement at PIDA

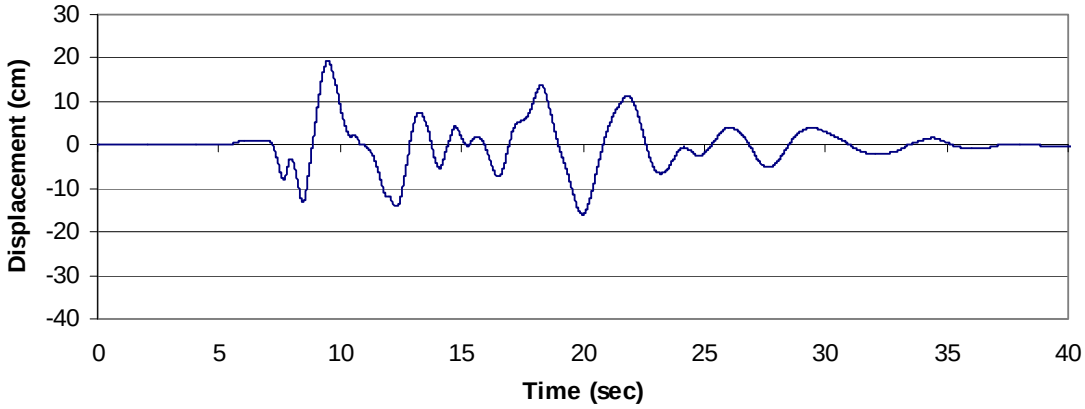

Figure 3-20: EW 32 meter time history of displacement at PIDA

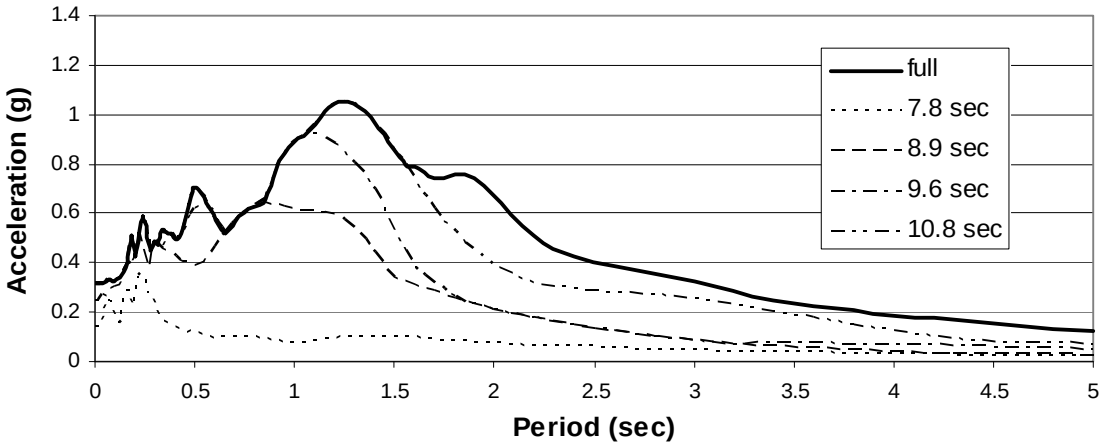

Figure 3-21: NS surface acceleration response spectra

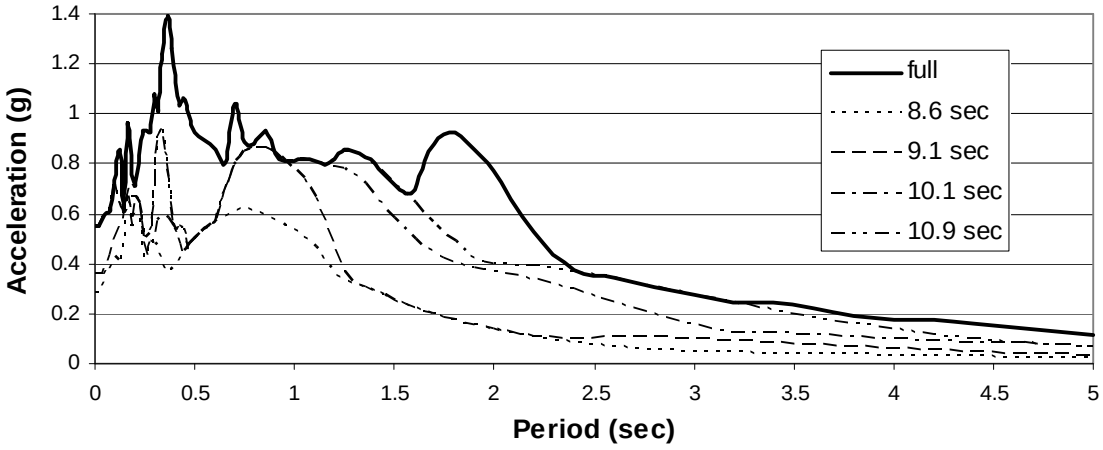

Figure 3-22: NS 16 meter acceleration response spectra

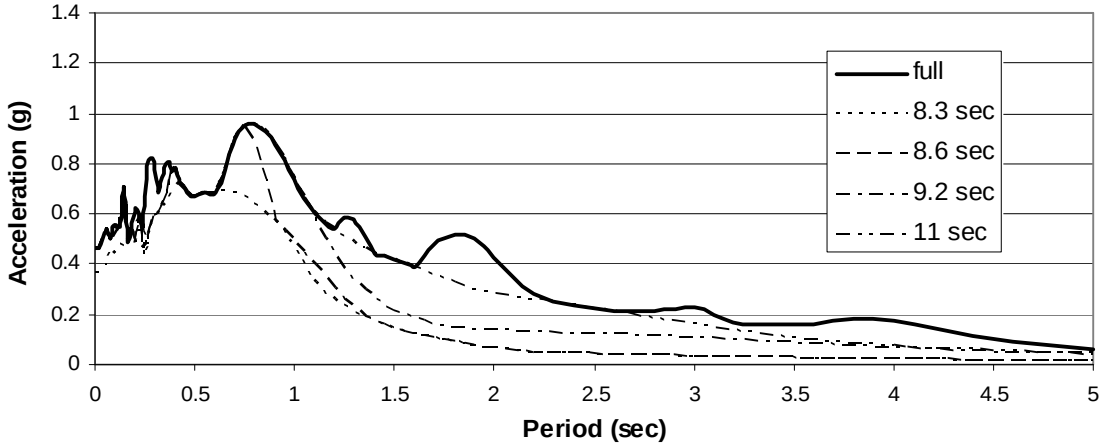

Figure 3-23: NS 32 meter acceleration response spectra

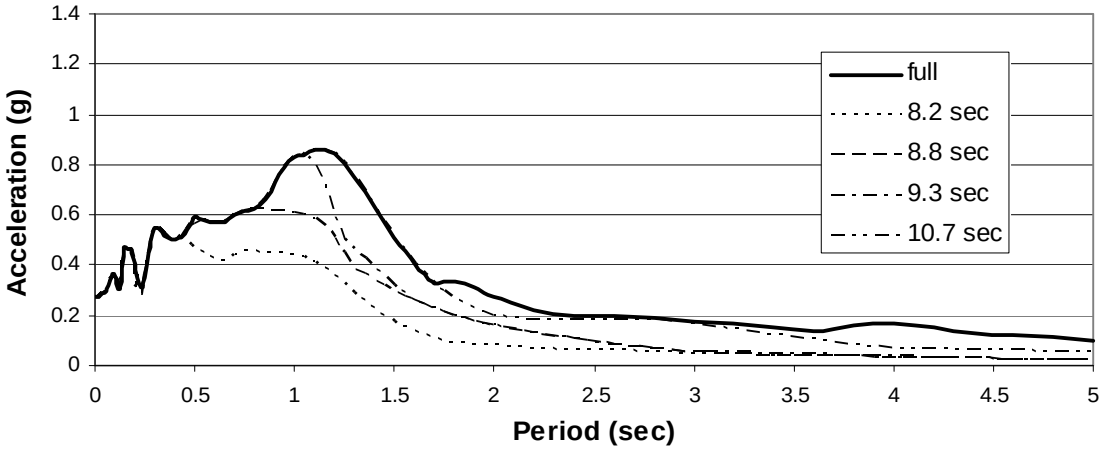

Figure 3-24: EW surface acceleration response spectra

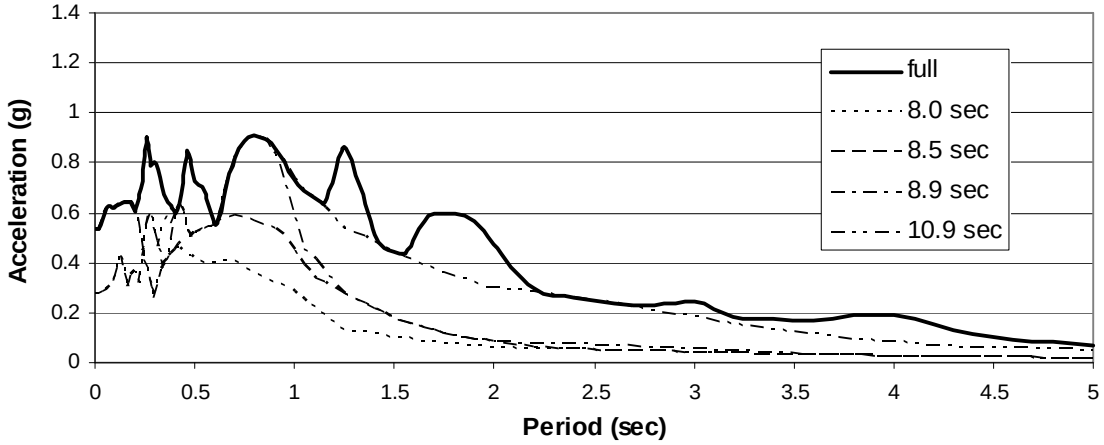

Figure 3-25: EW 16 meter acceleration response spectra

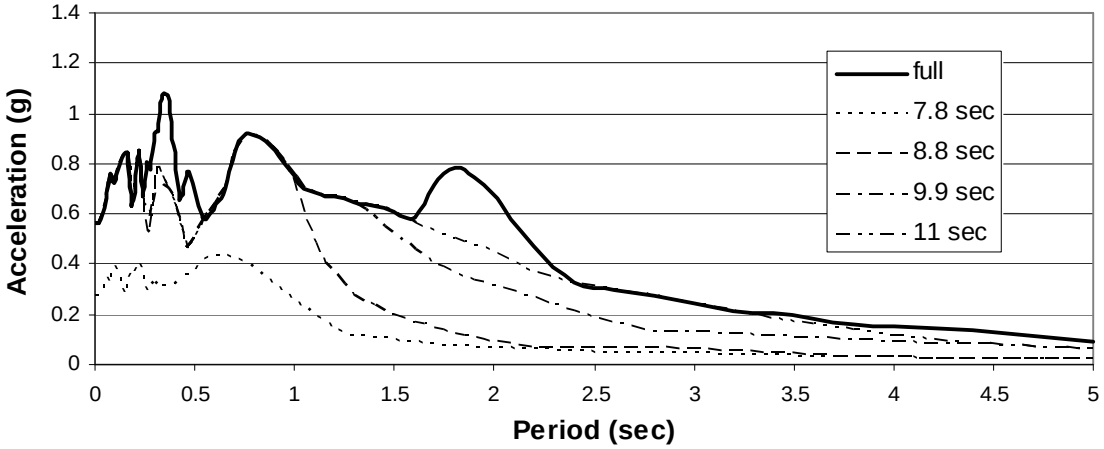

Figure 3-26: EW 32 meter acceleration response spectra

3.4 Study of PIDA Time Histories by Elgamal et al. (1996)

Elgamal et al. (1996) studied the ground motions recorded by the PIDA site during the Kobe Earthquake. Using a shear beam type of model and recorded ground accelerations, Elgamal et al. calculated shear stress time histories for points located between the accelerometers. Using double integrated accelerations to calculate the displacements of the accelerometers, Elgamal et al. determined shear strain time histories by dividing the differences in displacement between adjacent accelerometers by their horizontal spacing. In initially processing the ground motions, Elgamal et al. used a zero-phase time domain finite-duration impulse response (FIR) filter. This filter was used to correct a base line drift and smooth the stress time histories. The recorded accelerations were also reoriented so that they would correspond to planes of maximum and minimum horizontal shear stress. It should be noted that there is approximately a three second time difference in the time histories presented by Elgamal et al. and the time histories presented in this thesis, the latter having been previously processed by the Pacific Earthquake Engineering Research (PEER) Center.

The cyclic stress-strain plots created by Elgamal et al. are shown in Figure 3-27 and Figure 3-28. Figure 3-27 shows the entire stress-strain time history at depths of 8, 24, and 57.5 meters. These depths are at the midpoints of three layers bounded by the four accelerometers in the PIDA. The entire stress-strain time history is shown for both principal directions of stress. Figure 3-28 shows the stress-strain time history for the N44W direction, the plane of maximum shear stress. The stress-strain time history is broken up into time increments to show the progression of the soil degradation at the two shallower depths.

In interpreting these plots, Elgamal et al. concluded that below a depth of 32 m the soil response was essentially linear; this implies that below 32 m there was no significant loss of soil strength and no liquefaction. But above 32 m and especially at a shallower depth of 8 m (representing the average depth of the soil layer between 0 and 16 m), softening occurred. The notable and nearly complete flattening of the stress-strain loops at a depth of 8 m was a result of liquefaction.

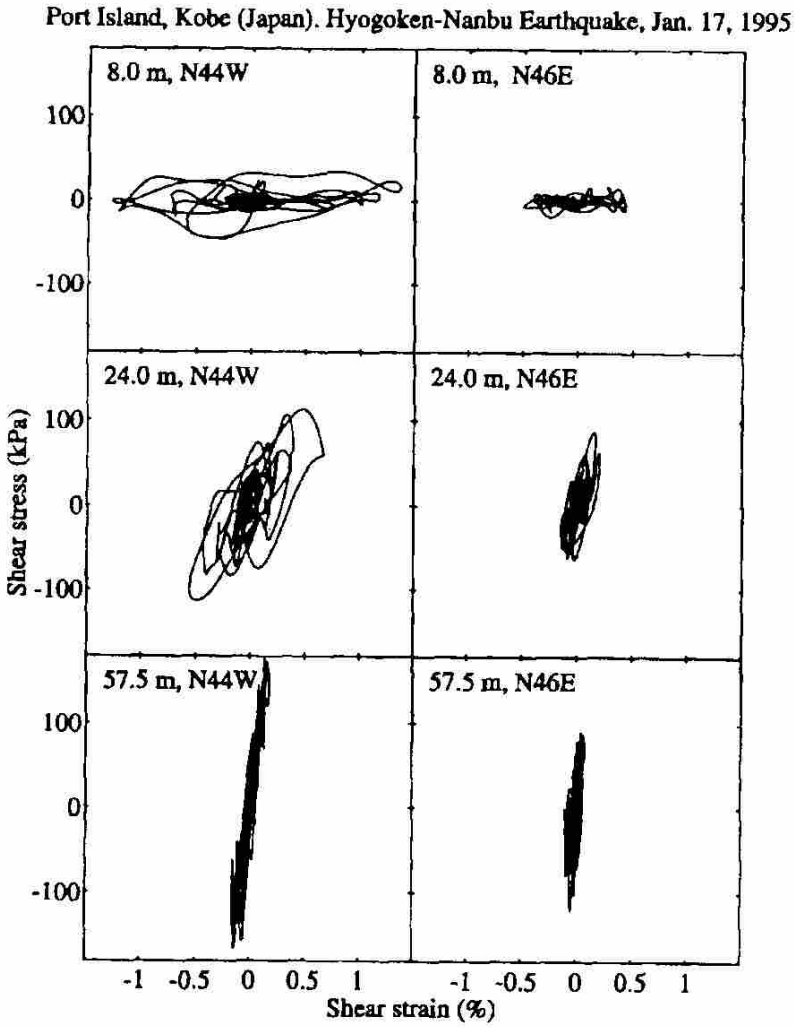

Figure 3-27: Full stress-strain plots, both directions, all depths (Elgamal et al., 1996)

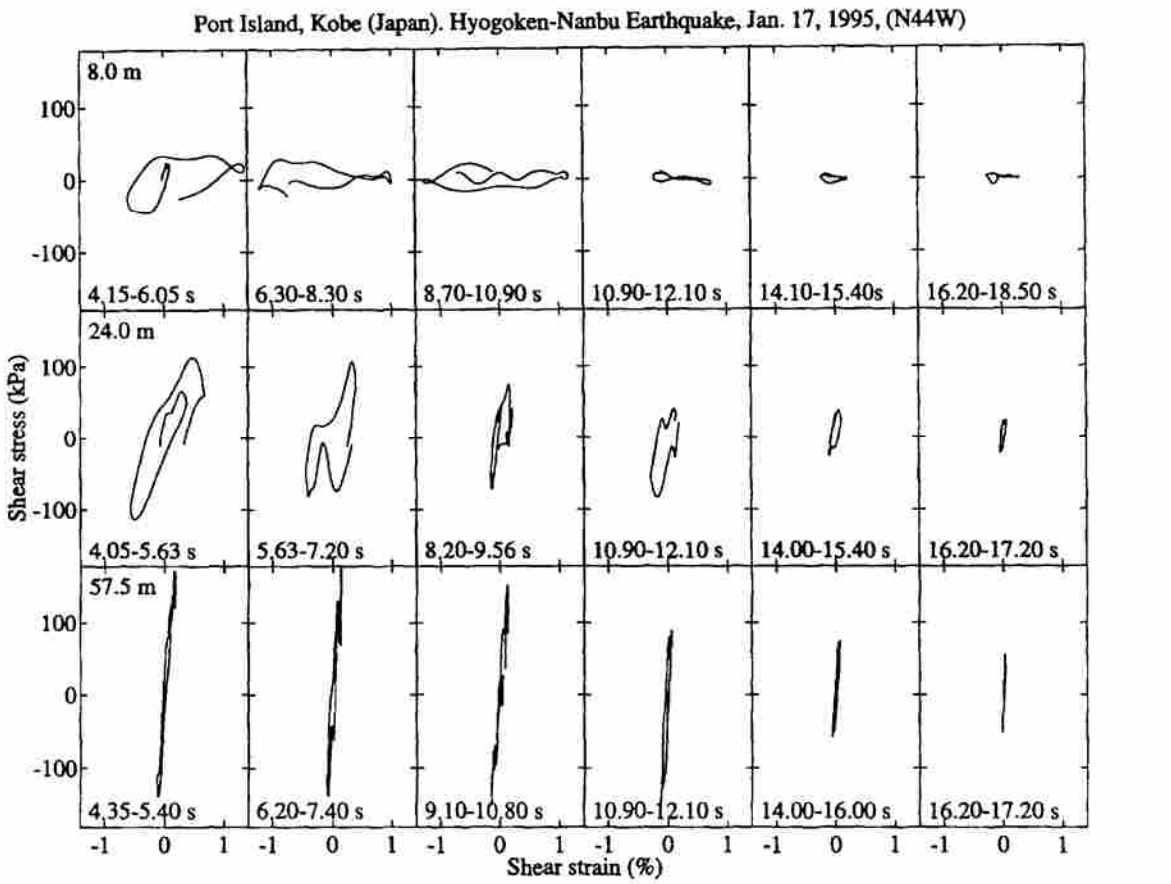

Figure 3-28: Incremental stress-strain plots at various depths (Elgamal et al., 1996)

While Elgamal et al. provides significant insight into the progression of liquefaction during an actual earthquake, their study does not clearly quantify how much the shear modulus degrades and what contributes to this degradation. Their study is helpful in analyzing after the event what happened during the earthquake; but, in order to better design structures for the effects of earthquakes, prediction of earthquake accelerations and soil strength during the earthquakes is essential. To predict ground motions in liquefiable soil during an earthquake, a specific method which quantifies the stress-strain behavior (or in other words, the shear modulus degradation) of the soil as it liquefies over time is needed.

3.5 Study of PIDA Time Histories by Youd and Carter (2003)

The current International Building Code does not explicitly specify design parameters for structures built on potentially liquefiable soils. For other soil types, coefficients are provided which are used to define an acceleration response spectrum. From this acceleration response spectrum, lateral forces can be determined to use in design of structures.

In an effort to provide guidance in defining acceleration response spectra representative of liquefiable soils, Youd and Carter (2003) used PROSHAKE to analyze the ground motions at sites where liquefaction occurred, including the PIDA site. Youd and Carter calculated acceleration response spectra for each site assuming non-liquefied soil properties. Youd and Carter then compared these theoretical spectra to the actual acceleration response spectra. Their results for the North-South and East-West components of ground motion are shown in Figure 3-29 and Figure 3-30.

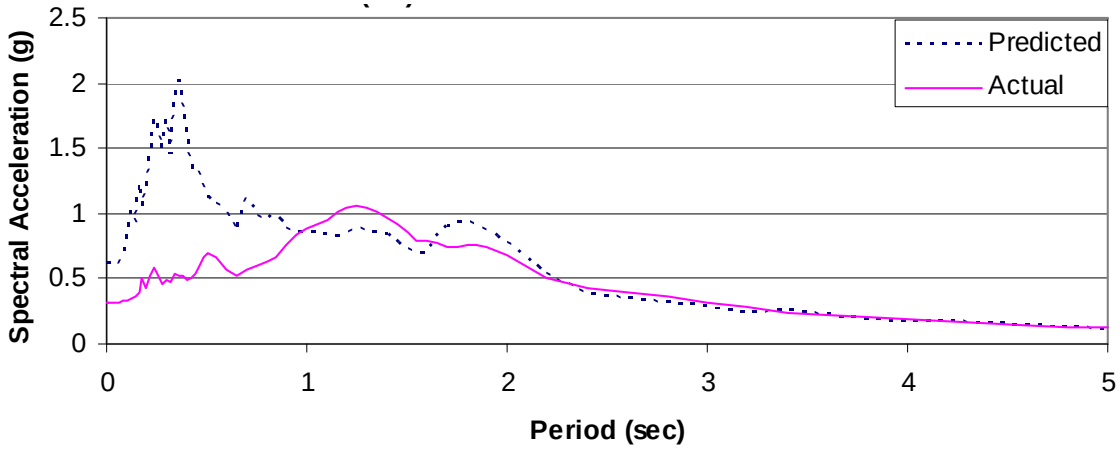

Figure 3-29: Response spectra for the PIDA site, N-S component, based on liquefied (actual) and non-liquefied (predicted) soil properties (Youd and Carter, 2003)

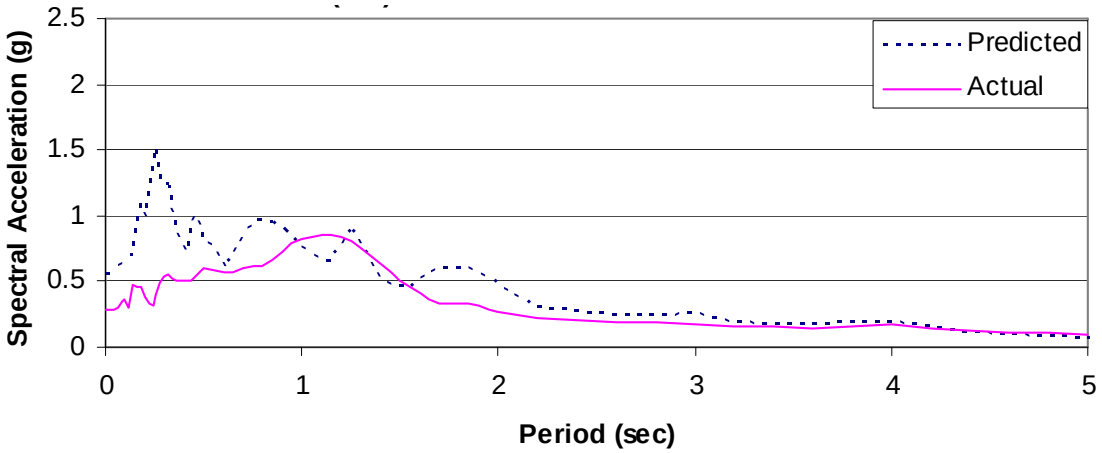

Figure 3-30: Response spectra for the PIDA site, E-W component, based on liquefied (actual) and non-liquefied (predicted) soil properties (Youd and Carter, 2003)

In comparing the spectral shapes for the PIDA and other sites, Youd and Carter focused on spectral response in terms of shorter periods of less than 0.7 seconds, and longer periods between 0.7 to 1.0 seconds. For shorter periods, there was actually a reduction in spectral accelerations when the earthquake-induced pore pressures rose rapidly. The accompanying soil softening reduced the spectral accelerations. When the pore pressures did not rise rapidly, there was little effect on the spectral accelerations. For longer periods, when soil softening occurred, there was an increase in spectral accelerations. In either case, Youd and Carter suggest that design procedures for potentially liquefiable sites need to account for large displacements that may occur during liquefaction, and that design procedures should not be limited to peak spectral accelerations.

4 Quantification of Shear Modulus in Liquefying Sand

4.1 Analytical Method

In order to ultimately model the shear stress-strain relationship of liquefying soil, time history data from the PIDA was analyzed to determine how shear stress varied with respect to shear strain during an actual earthquake. While similar analyses were performed by Elgamal et al. (1996), the analyses completed for this thesis are different with respect to several details.

Conceptually, the analyses performed are similar to the processes utilized by the nonlinear site response analysis program NERA. The difference is that rather than using soil properties and a base motion as inputs to find accelerations at different depths in the soil strata, the known PIDA accelerations are used to determine the stress-strain behavior of the soil (i.e., the shear modulus and damping of the soil are back-calculated from known time histories). Therefore, the analyses performed are similar to running the NERA program backwards.

While not explicitly stated earlier when describing the NERA-based algorithm, if ground acceleration at the surface is already known, a direct relationship exists between acceleration and shear stress. In the case of the PIDA site, since only the shear stress-strain behavior of the surface layer which liquefied is of interest, it is unnecessary to solve for the shear stress of the entire soil profile. The direct relationship between shear

stress and acceleration is defined by combining Equations 4.1 and 4.2 and solving for shear stress as shown in Equation 4.3.

$$\widetilde{v}_{1,n+1} = \widetilde{v}_{1,n} + \left(\frac{2\tau_{1,n}}{\Delta z_1}\right)\left(\frac{\Delta t}{\rho_1}\right) \quad \textbf{(4.1)}$$

$$a_{i,n} = \frac{1}{\Delta t}(\widetilde{v}_{i,n+1} - \widetilde{v}_{i,n}) \quad \textbf{(4.2)}$$

$$\tau_{1,n} = \frac{1}{2} a_{1,n} \Delta z_1 \rho_1 \quad \textbf{(4.3)}$$

where $\widetilde{v}$ is the predicted nodal velocity for the respective node (i.e., top of the respective layer) and time step, τ is the shear stress for the respective layer and time step, ρ_i is the unit density of layer i, Δz is the thickness of the specified layer, and Δt is the time step increment or interval, and a is the acceleration for the respective node and time step. In Equation 4.3, shear stress is uniquely a function of the acceleration of the ground surface, as well as the thickness and unit density of the layer.

Shear strain is found by double integrating the recorded acceleration time histories at the top and bottom of the layer to obtain displacement and then applying Equation 4.4.

$$\gamma_{i,n} = \frac{d_{i+1,n} - d_{i,n}}{\Delta z_i} \quad \textbf{(4.4)}$$

where d is the displacement, Δz is the layer thickness, and γ is the shear strain at the respective layer and time step increment. When calculating stress and strain, a layer thickness of either 16 or 12 m could be used. The 16 m value is based on the difference in depth between the two uppermost accelerometers where data was recorded. The 12 m value is based on the thickness of liquefiable soils between the two accelerometers. When the soil liquefies and loses stiffness, most of the strain in the profile will occur within the liquefied 12 m interval. In this situation, the non-liquefied soil above the water table would act as a 4-m thick crust experiencing approximately the same acceleration at the ground surface as at a depth of 4 m. In reality, the most appropriate layer thickness is one that varies from 16 to 12 m during the liquefaction process. Because of this thesis' focus on the modulus of liquefying soil and the uncertainty of exactly how the thickness value would vary with time, a constant layer thickness of 12 m was used with the understanding that the actual moduli before and during the initial stages of liquefaction could be up to 78% larger. (This value comes from the ratio of the square of 16/12; layer thickness is in numerator of Equation 4.3 and in the denominator of Equation 4.4, and the ratio of these two equations is shear modulus).

When using the NERA-based algorithm, consideration must be given to the stiffness and thickness of the soil being analyzed because these parameters dictate the fundamental frequency or period of the soil layer. The effects of a ground motion's components with frequencies higher than the fundamental frequency (or periods lower than the fundamental period) cannot be fully accounted for in the analysis. The maximum frequency, f_{max}, that can be fully accounted for in the analysis is shown in Equation 4.5.

$$f_{\max} = \frac{V_s}{4H} \tag{4.5}$$

where V_s is the shear wave velocity and H is the thickness of the soil layer. For the 12 m-thick liquefiable soil layer, the maximum frequency is approximately 4.4 Hz, which corresponds to a period of 0.23 sec. (If a 16 m thickness were used, the frequency and period would be 3.3 Hz and 0.3 sec, respectively). Figure 4-1 and Figure 4-2 show the Fourier amplitude spectra (computed from the recorded time histories using PROSHAKE) for the accelerations occurring in the North-South and East-West directions, respectively, at depths of 0 and 16 m. It can be seen that these accelerations are mostly comprised of frequency components less than the calculated maximum frequency, meaning that the results from the NERA-based algorithm should reasonably represent the stress-strain behavior of the soil at the site.

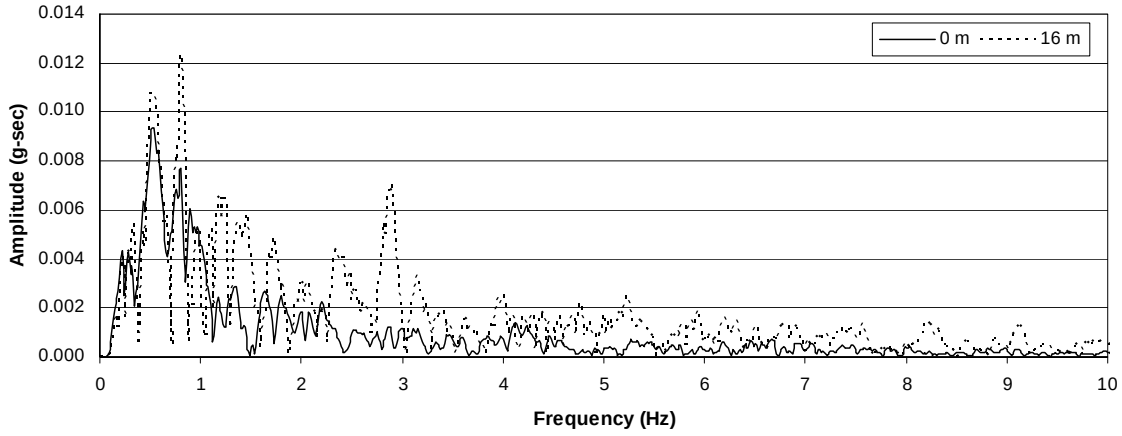

Figure 4-1: Fourier amplitude spectra of acceleration at 0 and 16 m depths, NS

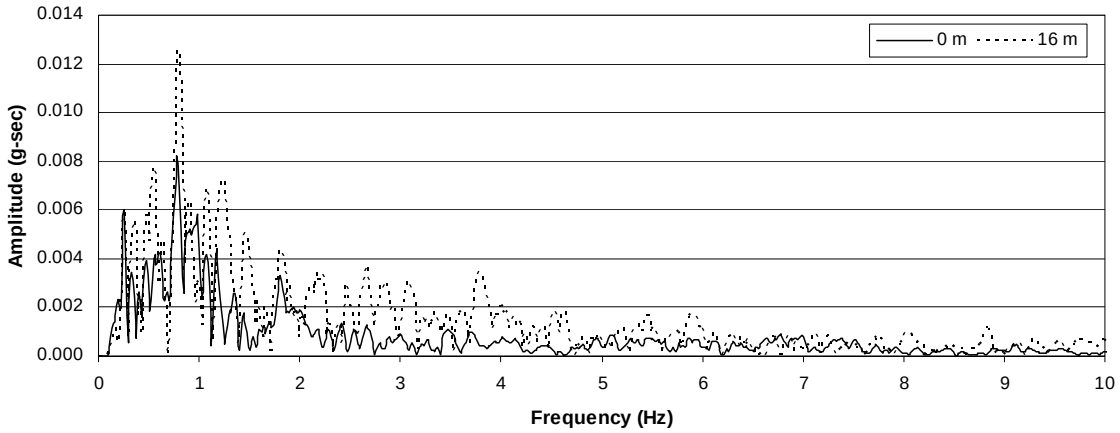

Figure 4-2: Fourier amplitude spectra of acceleration at 0 and 16 m depths, EW

4.2 Results and Interpretation of Results

The calculated shear stress and shear strain time histories for the North-South (NS) direction are presented in Figure 4-3 and Figure 4-4. The calculated shear stress and shear strain time histories for the liquefiable soil layer were plotted together to get the whole time history of the stress-strain relationship for the North-South direction. The combined shear stress-strain plot can be seen in Figure 4-5.

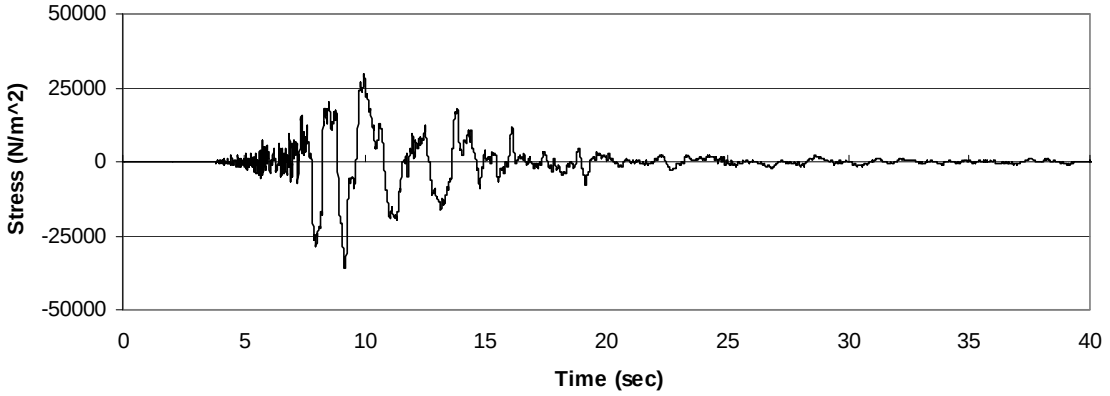

Figure 4-3: Shear stress time history for the liquefiable soil layer, NS

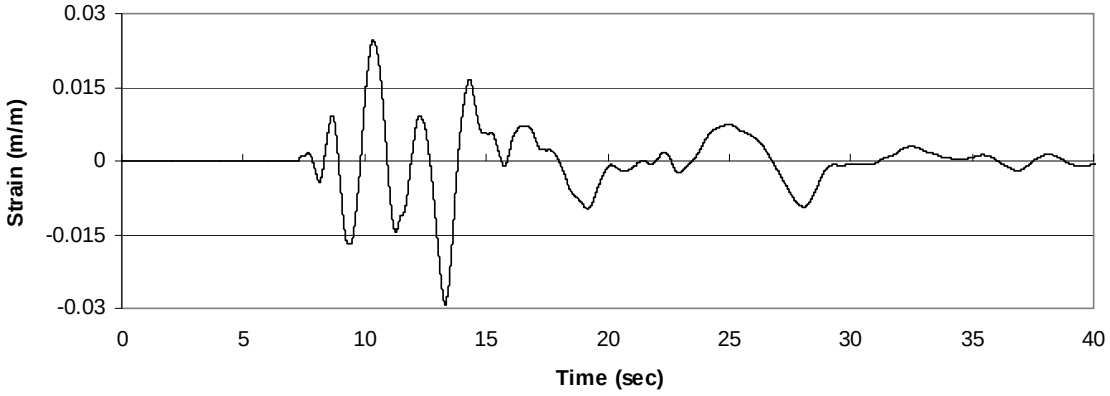

Figure 4-4: Shear strain time history for the liquefiable soil layer, NS

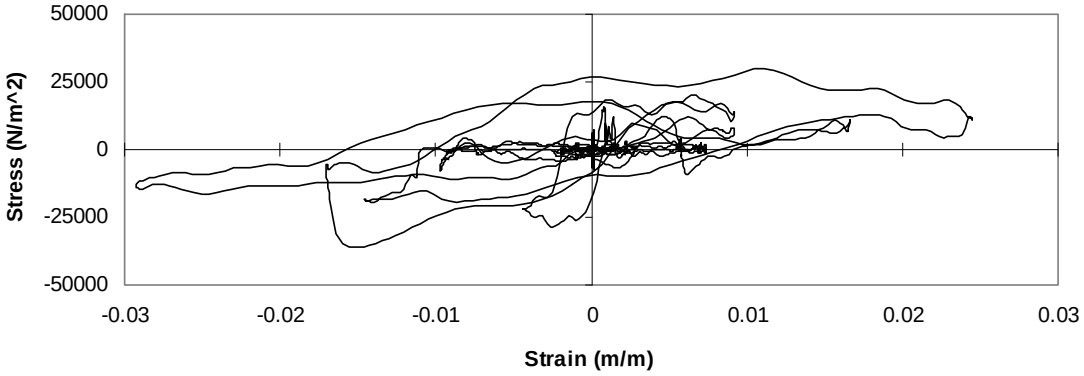

Figure 4-5: Shear stress-strain plot for the liquefiable soil layer, NS

For improved viewing, four individual hysteretic loops from the continuous stress-strain plot in Figure 4-5 are presented in Figure 4-6 through Figure 4-9. The time duration for each of the hysteretic loops varies from approximately 1.0 to 2.1 seconds. The hysteretic loop for 7.3 to 8.3 seconds shown in Figure 4-6 has a shear modulus of approximately 6.2 MN/m^2 (as compared to an initial, low-strain shear modulus of 86 MN/m^2 derived from the measured shear wave velocity). The shear modulus continues to degrade as time progresses. The last hysteretic loop from 11.9 to 13.8 seconds is shown

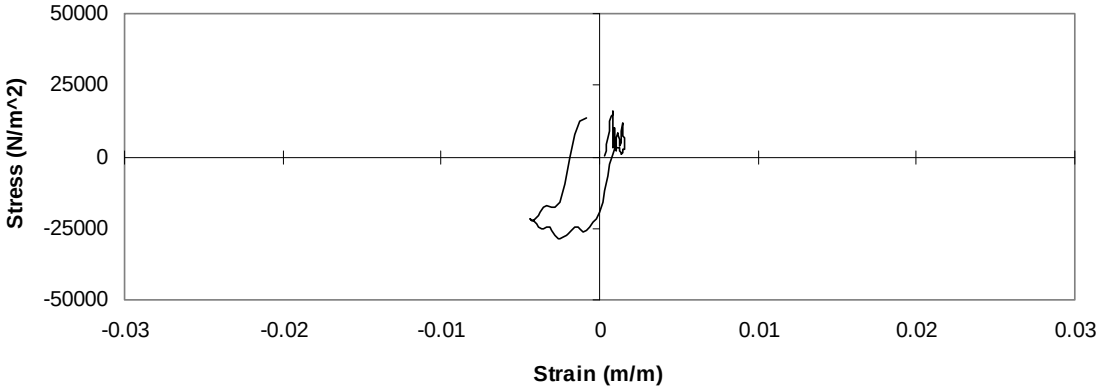

Figure 4-6: Stress-strain hysteretic loop from 7.3 to 8.3 seconds, NS

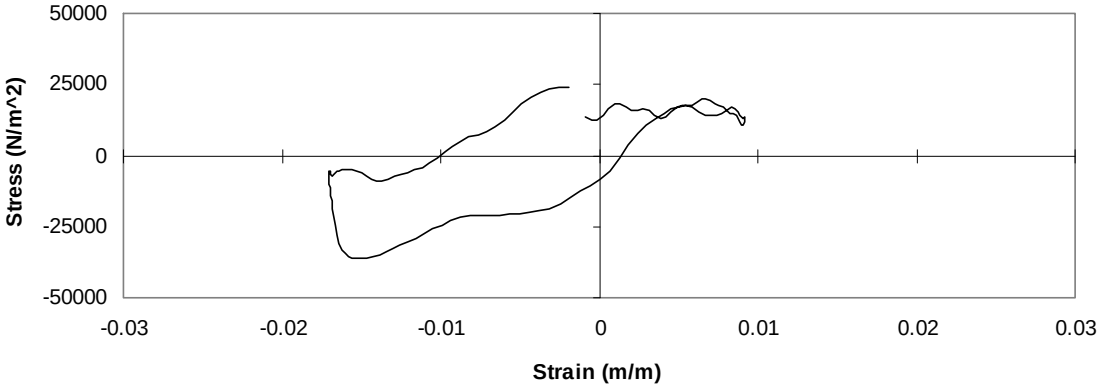

Figure 4-7: Stress-strain hysteretic loop from 8.3 to 9.8 seconds, NS

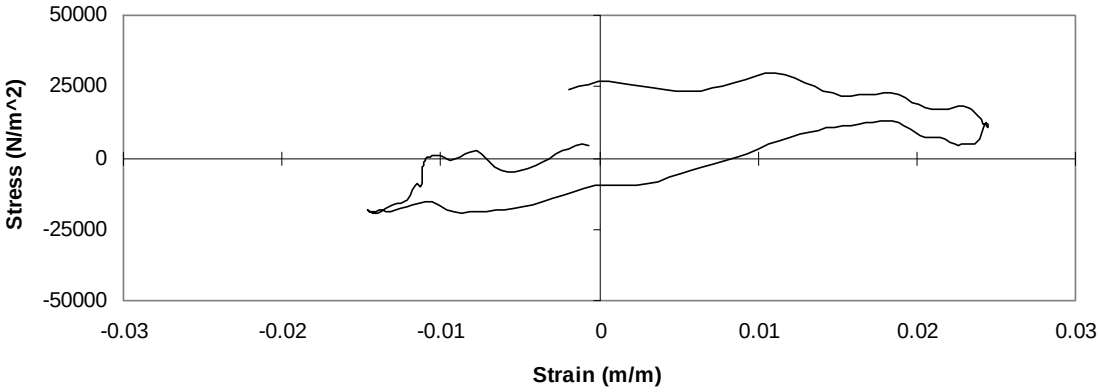

Figure 4-8: Stress-strain hysteretic loop from 9.8 to 11.9 seconds, NS

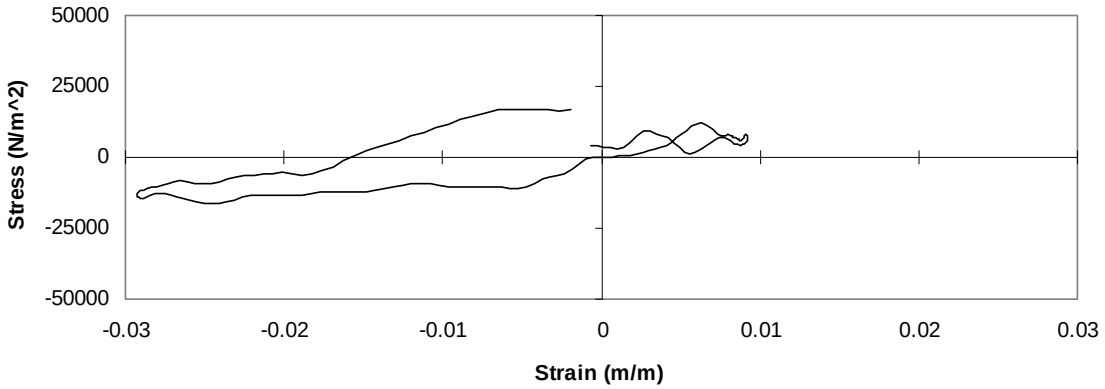

Figure 4-9: Stress-strain hysteretic loop from 11.9 to 13.8 seconds, NS

in Figure 4-9. The shear modulus for this loop has degraded to approximately 0.5 MN/m^2.

The calculated shear stress and shear strain time histories from the East-West (EW) component are presented in Figure 4-10 and Figure 4-11. The calculated shear stress and shear strain time histories for the liquefiable soil layer were plotted together to get the whole time history of the stress-strain relationship. The combined shear stress-strain plot can be seen in Figure 4-12.

For improved viewing, four hysteretic loops from the continuous stress-strain plot in Figure 4-12 are presented in Figure 4-13 through Figure 4-16. The time duration for each of the hysteretic loops varies from approximately 1.1 to 2.1 seconds. The hysteretic loop for 7.2 to 8.3 seconds shown in Figure 4-13 has a shear modulus of approximately 6.5 MN/m^2, while the last hysteretic loop from 11.8 to 13.8 seconds has a shear modulus of approximately 0.5 MN/m^2. This trend is the same as that observed in the North-South direction.

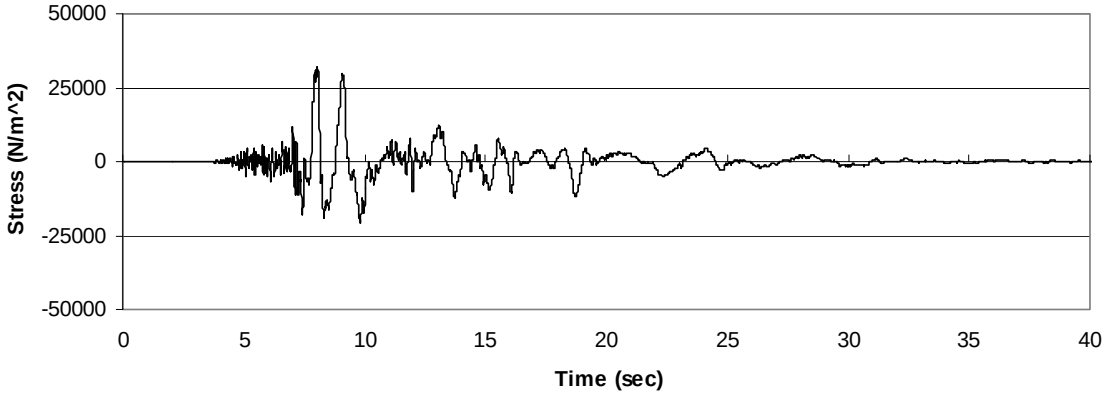

Figure 4-10: Stress time history for the liquefiable soil layer, EW

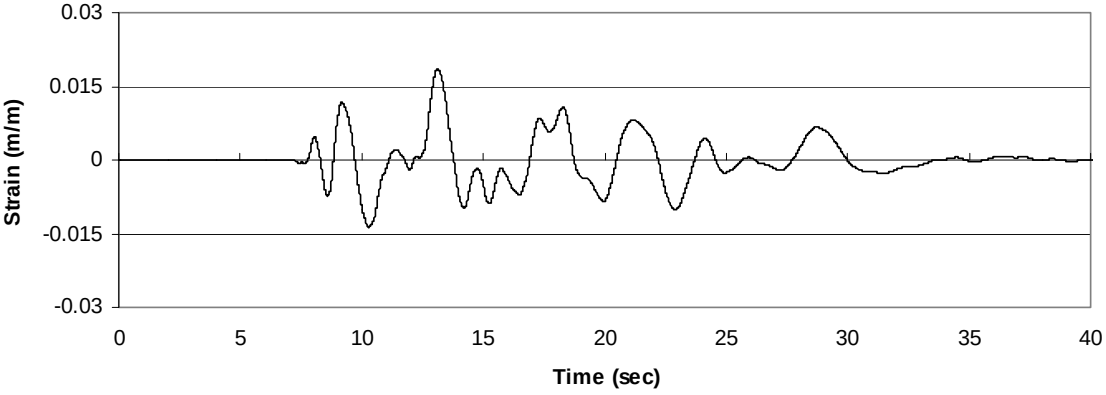

Figure 4-11: Strain time history for the liquefiable soil layer, EW

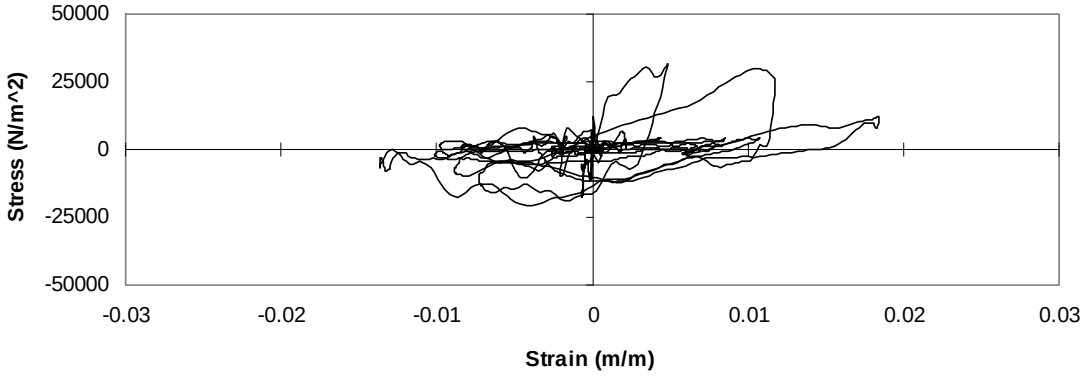

Figure 4-12: Shear stress-strain plot for the liquefiable soil layer, EW

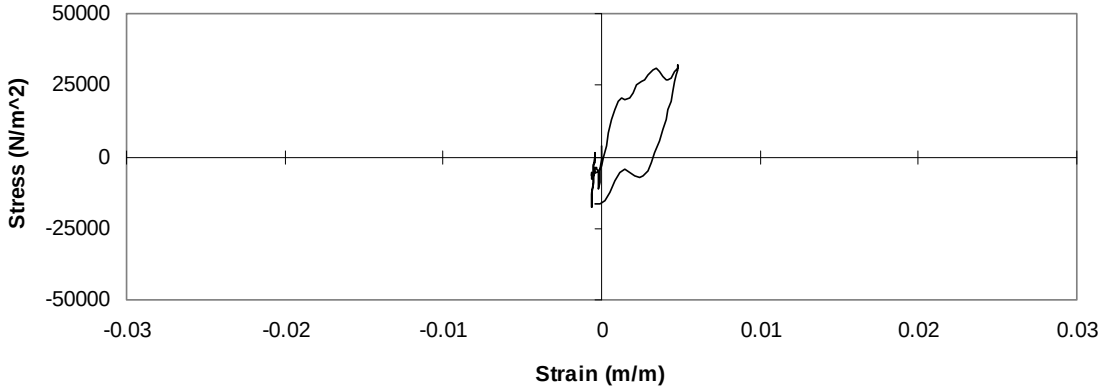

Figure 4-13: Stress-strain hysteretic loop from 7.2 to 8.3 seconds, EW

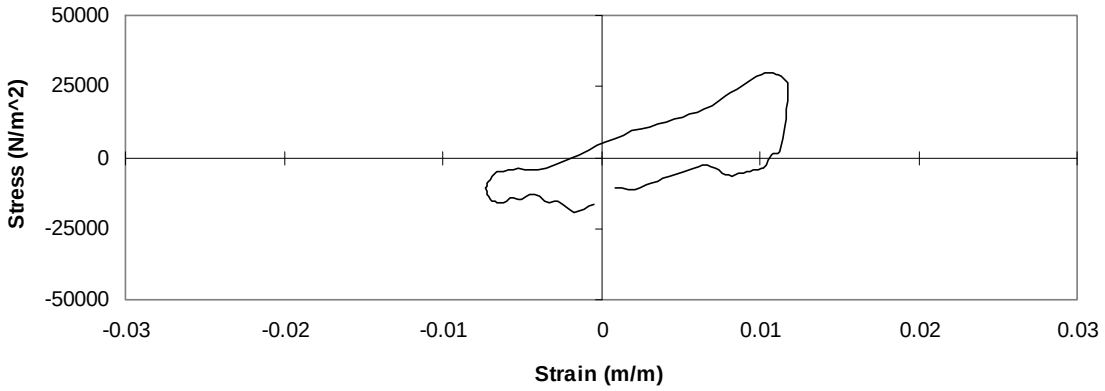

Figure 4-14: Stress-strain hysteretic loop from 8.3 to 9.7 seconds, EW

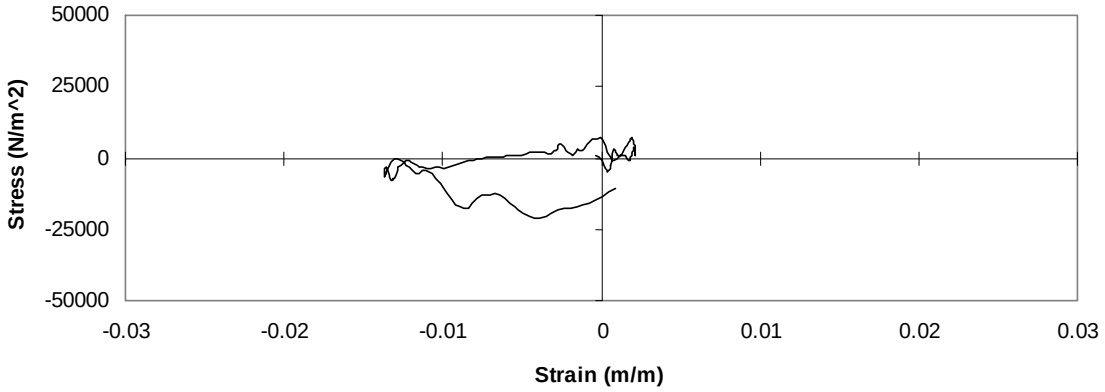

Figure 4-15: Stress-strain hysteretic loop from 9.7 to 11.8 seconds, EW

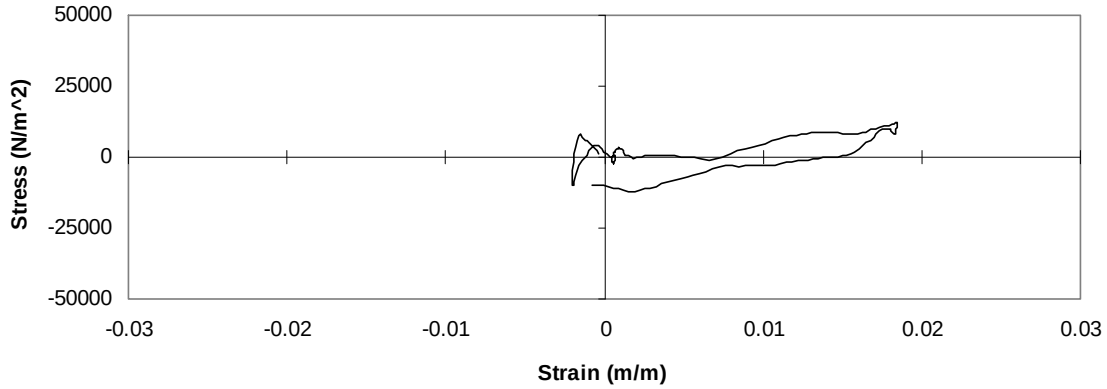

Figure 4-16: Stress-strain hysteretic loop from 11.8 to 13.8 seconds, EW

In comparing the stress-strain loops presented in this thesis with those of Elgamal et al., (1996) certain differences are noted. These differences derive from several sources. First, the manner in which the original PIDA data was processed to remove extraneous frequencies and correct for drift is different. Second, Elgamal et al. rotated the orientation of the measured components of motion into minimum and maximum axes; the stress-strain hysteretic loops presented here have not been reoriented. Third, Elgamal et al. used a shear beam model to calculate shear stress. A shear beam model uses accelerations from the top and bottom of the beam (or soil layer) to compute stresses whereas the formulation used to determine shear stress in this thesis uses only the acceleration at the top of the soil layer. Both methods are valid, although the shear beam is more rigorous. Associated with this issue is the layer thickness used to calculate shear stresses and shear strains. Elgamal et al. used a constant 16 m thickness while a constant 12 m thickness has been used in this thesis for the reasons discussed previously.

Shear strain and shear modulus were calculated for each hysteretic half-loop during the earthquake stress-strain time history. Half-loops were used rather than full loops in order to better capture shear modulus degradation during the rapid softening of

the soil. Shear strain and shear modulus were determined using peak values from the half-loop, and in the case of shear modulus, was calculated using the origin-to-endpoint slope of the stress-strain half-loop. The half-loop shear strains from the North-South (NS) direction are plotted as a function of time in Figure 4-17 and the corresponding half-loop shear moduli are plotted in Figure 4-18. Similar plots for the East-West (EW) direction are shown in Figure 4-19 and Figure 4-20. Horizontal lines with endpoints are used to represent the range of time over which the modulus was computed. Endpoints were selected such that they coincided with near-zero strains before and after peak shear stresses. The 86 MN/m^2 line represents what the maximum shear modulus should be according to a representative shear wave velocity of 210 m/sec and a mass density of 1950 kg/m^3, which are values based on measured site data. The dashed lines represent approximate trendlines based on all of the hysteretic loops.

The general trends shown in Figure 4-17 through Figure 4-20 indicate that the shear modulus of the liquefiable layer changes dramatically during the earthquake. There is a rapid reduction in shear modulus (or in other words there is a significant soil softening) beginning at approximately 7 seconds. A comparison with the anticipated reduction in shear modulus based on Seed and Idriss' (1970) average shear modulus reduction curve for sand indicates that the observed decrease is more than that expected due to reduction of the shear modulus with increasing cyclic strain alone. The difference is attributable to the effects of liquefaction.

As the soil liquefies, the shear modulus degrades approximately two orders of magnitude until a relatively constant value of 1% of G_o is reached at approximately 13 second (although most of the reduction occurs by 9 to 10 seconds). Corresponding shear

strains are on the order of 1 to 2%. This reduced shear modulus for liquefied sand equals approximately 15% of the shear modulus value from Seed and Idriss' average sand curve.

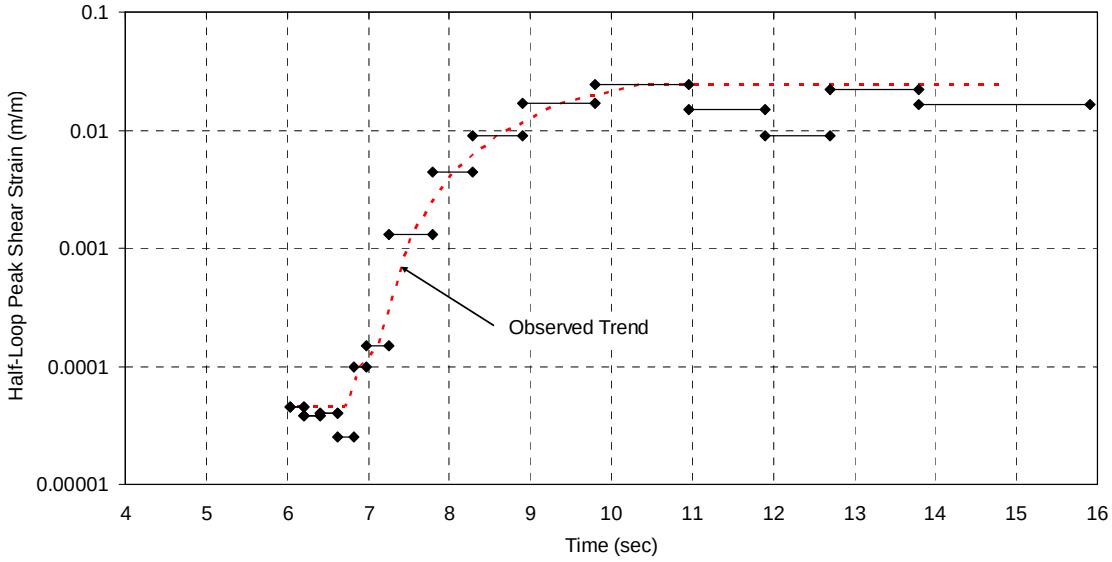

Figure 4-17: Time history of half-loop shear strain for the liquefiable layer, NS

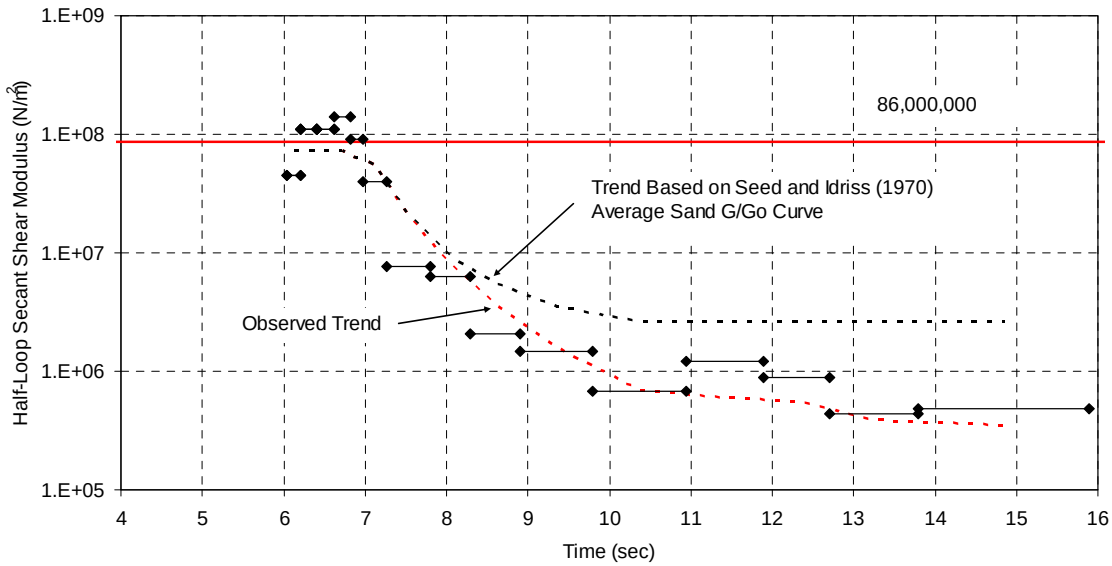

Figure 4-18: Time history of half-loop shear modulus for the liquefiable layer, NS

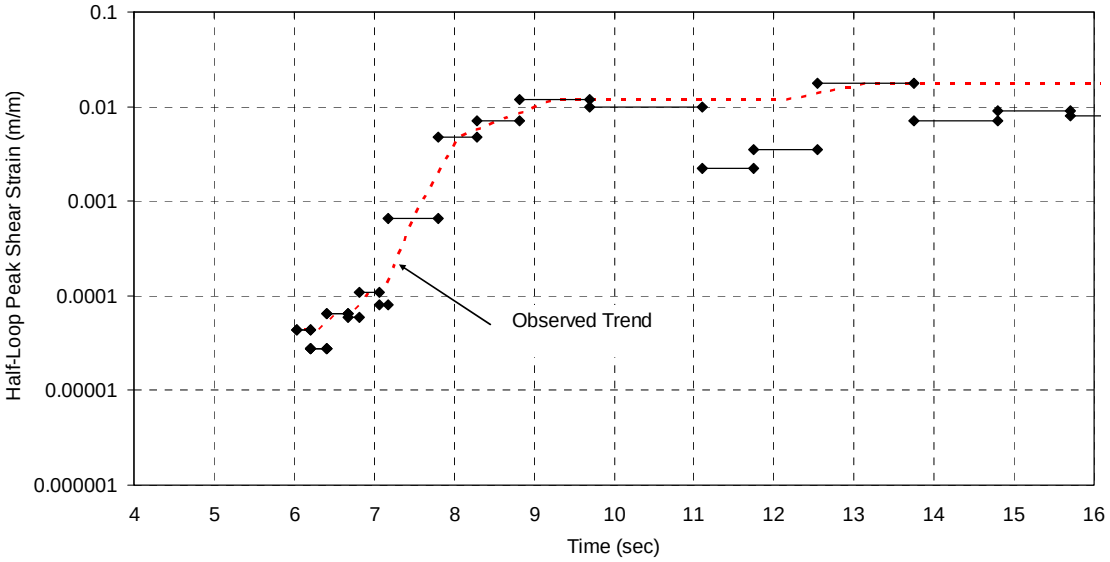

Figure 4-19: Time history of half-loop shear strain for the liquefiable layer, EW

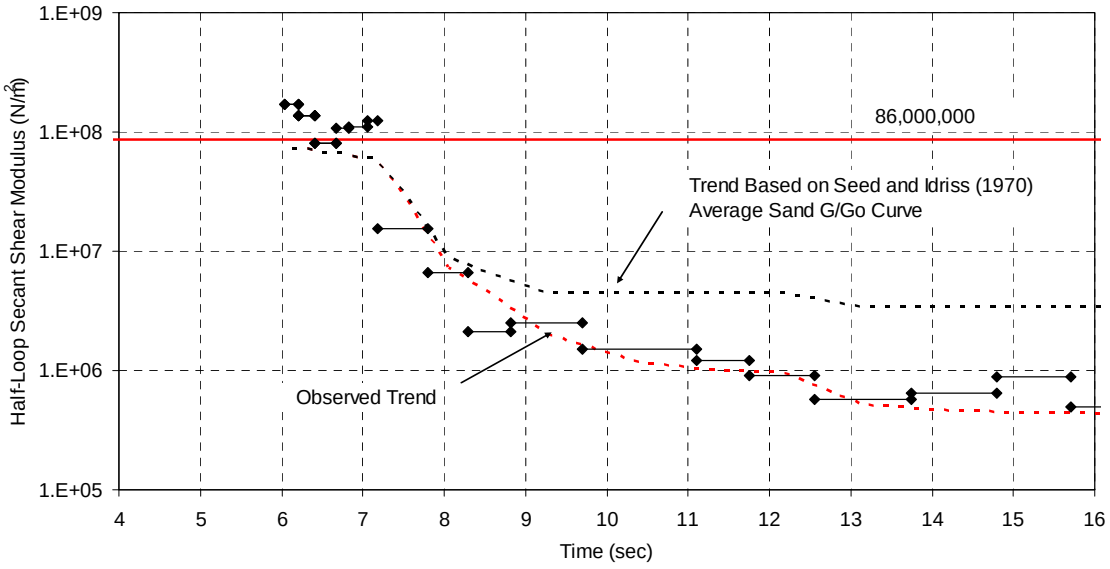

Figure 4-20: Time history of half-loop shear modulus for the liquefiable layer, EW

In the figures, there are several calculated moduli larger than G_o prior to 7 seconds. These higher shear modulus values are explained by difficulties in precisely

defining a hysteretic loop with very low strain levels together with noise in the time histories.

Unfortunately, since the moduli shown in Figure 4-18 and Figure 4-20 are only equivalent shear moduli, the data insufficiently describes the complete shear stress-stain behavior of the soil (i.e., behavior during both loading prior to peak strain and unloading afterward). Such information might be sufficient for an equivalent linear analysis using the computer program PROSHAKE; however, due to the dramatic loss of shear strength, it is impossible to accurately represent the soil with a single "equivalent" modulus throughout the entire time history. PROSHAKE analyses were performed to confirm this. In these analyses, the equivalent shear moduli from the time history combined with the respective strains to form a shear modulus curve. These analyses produced an acceleration response spectrum which greatly underestimated the actual response. This under-estimation occurred because even with a strain ratio factor of 0.65 being applied to the maximum strain in the time history, the resulting "representative" shear strain was sufficiently large that the corresponding shear modulus used in the analysis was very small. Because of this, the computed ground motions occurring before and during the onset of complete liquefaction did not contribute to the response spectra to the same degree as the actual ground motions did.

5 Modeling of Shear Modulus in Liquefying Sand

5.1 Conceptual Approach

In order to perform a seismic ground response analysis for a site with liquefiable soil, another analytical method different than the equivalent linear model and the PROSHAKE computer program is needed. The ability to model individual shear stress-strain loops should help to more accurately predict ground motions. Such modeling can be accomplished by using a time domain analysis with a non-linear Iwan-Mroz model (as used with the NLM in NERA) whose incremental stiffness conforms to some backbone shear modulus degradation curve. However, in the case of liquefiable soils, not only does the stiffness of a soil decrease as a function of strain as with normal soils, the stiffness also decreases due to liquefaction itself and the development of excess pore water pressure. Because of this compounding decrease in stiffness, it would be beneficial to have a shear modulus degradation curve which can be reduced as a soil undergoes liquefaction, which then updates the Iwan-Mroz model to reflect these changes. This approach is referred to in this thesis as the "degrading backbone curve model" (and is not incorporated as a part of NERA). In this chapter, an approach for formulating a degrading backbone curve is presented, and then such a curve is used to model the ground behavior observed at the PIDA site.

5.2 Development of a Degrading Shear Modulus Backbone Curve

5.2.1 Selection of Initial *G/Gmax* Curve

In the development of a degrading shear modulus backbone curve, the first step is to select a base G/G_{max} curve. For the PIDA site, the "average" shear modulus degradation curve for sand developed by Seed and Idriss (1970) is used. This curve was shown previously as Figure 2-2. This curve is used in the model for two reasons. First, despite common references to the reclaimed fill at Port Island as being gravelly, the mean grain size reported by Ishihara et al. (1998) is 2 mm or less. This grain size is more consistent with sand. In addition, work by Rollins et al. (1998) shows that G/G_{max} versus cyclic shear strain curves for gravels derived from 15 other investigations are more consistent with the Seed and Idriss (1970) sand curves than with the gravel curve reported by Seed et al. (1986).

5.2.2 Degradation of *Gmax* Due to Liquefaction

The initial G/G_{max} curve is assumed to degrade as excess pore water pressures develop during ground shaking and subsequent liquefaction of the soil. The relationship between the degradation of shear modulus and the development of excess pore water pressures is assumed to be similar to both the increase in the coefficient of volume compressibility, m_v and the reduction of the tangent rebound modulus, E_r with increasing pore pressure ratio as shown by Martin and Seed (1979) in Figure 5-1. This assumption seems valid given that G, m_v, and E_r, are all inter-related deformation constants. By inverting the ordinate of Figure 5-1, the scalar reduction of G as a function of peak (or

excess) pore pressure ratio is given directly. The inverted ordinate is referred to in this thesis as the "modulus scaling factor."

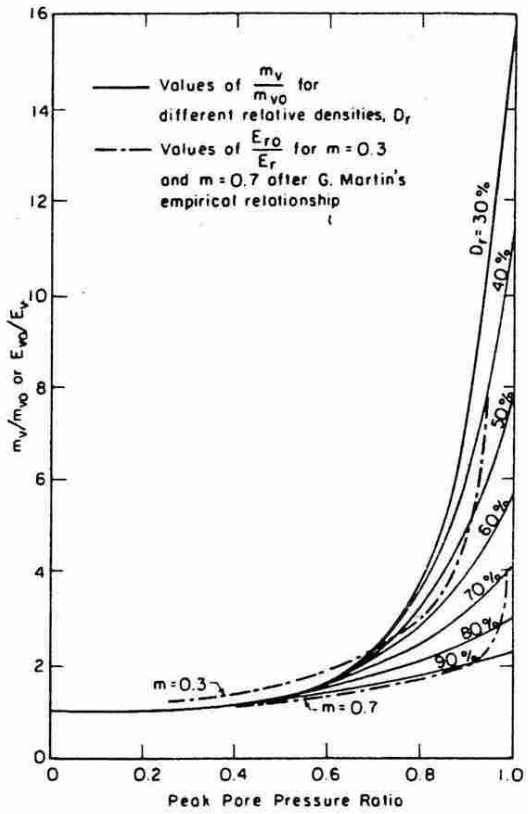

Figure 5-1: Theoretical relationships between compressibility of sands and pore-pressure buildup (Martin and Seed, 1979).

In the work associated with this thesis, the excess pore water pressure ratio, R_u, is defined as shown in Equation 5.1:

$$R_u = \frac{\Delta u}{\sigma_v^{'}} \qquad \textbf{(5.1)}$$

where Δu is the increase in pore water pressure due to dynamic loading and $\sigma_v^{'}$ is the initial effective vertical stress prior to liquefaction. It is interesting to note that when the ordinate of Figure 5-1 is inverted to obtain the modulus scaling factor (or modulus ratio),

the change in stiffness or modulus with increasing pore water pressure appears to be relatively linear. In the relative density range of 40 to 50% (which is representative of the reclaimed fill at the PIDA site), the modulus ratio varies from approximately 1 at R_u = 0.2 to approximately 0.125 at R_u = 1.0. A modulus ratio of 1 implies no loss in stiffness or modulus. These observations generally correlate with observations of the modulus degradation ratio from blast liquefaction testing at Treasure Island, California (Jelinek, 2000) and Maui, Hawaii (Rollins et al., 2004).

5.2.3 Backbone Curves as a Function of Excess Pore Pressure Ratio

By multiplying the shear modulus of the soil, G, by the modulus scaling factor, a set of shear modulus degradation curves can be obtained for different excess pore water pressure ratios, R_u. A few representative degradation curves are presented in Figure 5-2. These curves should be representative of "average" liquefiable sands with initial relative densities in the range of 40 to 50%. An alternate presentation of these curves in terms of shear stress-strain curves (with a value of G_{max} (also referred to as G_o) equal to 86 MN/m^2) is shown in Figure 5-3.

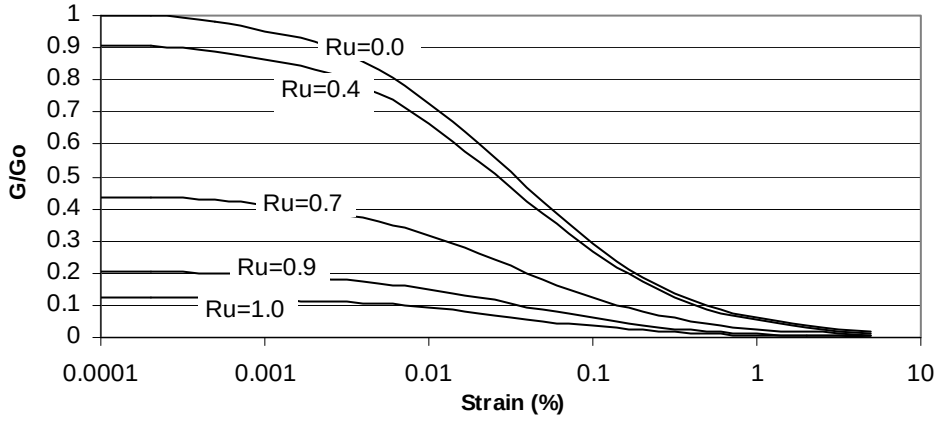

Figure 5-2: Shear modulus backbone curves as a function of excess pore pressure ratio

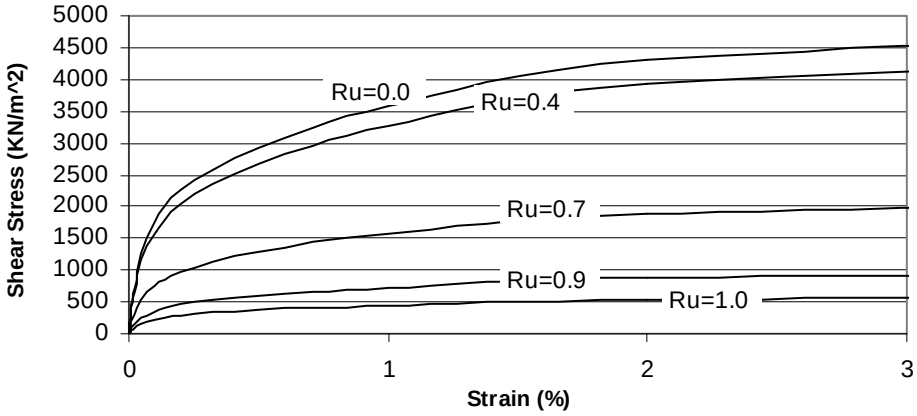

Figure 5-3: Shear modulus backbone curves as a function of excess pore pressure ratio

5.3 Calculation of Shear Stress-Strain Time Histories

To assess the effectiveness of the degrading backbone model just described, a shear stress time history was computed for the liquefying sand layer at the PIDA site. If a good match could be obtained between the shear stresses computed using the model and those determined previously in Chapter 4 using the recorded ground accelerations, the degrading backbone model would be validated (at least for the PIDA site). Calculation of the shear stress time history was accomplished by using the adapted NERA method described previously in Section 4.2, except that the analysis was conducted in its original forward direction, using an incremental strain time history to predict the corresponding stress time history. The incremental strain time history used is the actual strain time history from both the N-S and E-W components shown in Figure 4-4 and Figure 4-11. However, to incorporate the degrading backbone curve into the parameters of the Iwan-Mroz model, an estimate of the excess pore water pressure ratio for the liquefying sand is needed at each time step.

5.3.1 Excess Pore Water Pressure Ratio Time History

No pore water pressure data was recorded at the PIDA site. In order to develop an estimate of the excess pore water pressure ratio developed during liquefaction, Byrne's method (1991) of relating the accumulation of cyclic shear strain to volumetric strain was combined with Dobry and Ladd's relationship (1980) between cyclic shear strain and excess pore pressure ratio.

In Byrne's method, volumetric strain, in percent, due to self-compaction during and following cyclic strain is calculated by using Equation 5.2:

$$\left(\Delta\varepsilon_v\right)_{1/2\,cycle} = 0.5\gamma C_1 EXP\left(-C_2\frac{\varepsilon_v}{\gamma}\right) \qquad \textbf{(5.2)}$$

where γ is the amplitude of a half cycle shear strain, C_1 and C_2 are coefficients equal to 0.56 and 0.714, respectively, for a relative density of approximately 45%, ε_v is the accumulated volumetric strain from previous cycles in percent, and $\Delta\varepsilon_v$ is the increment of volumetric strain in percent per half cycle of shear strain. The accumulated volumetric strain can then be related to a change in pore water pressure as will be described later.

To use Byrne's model and calculate the volumetric property of pore water pressure, the two orthogonal (isotropic) components of ground motion need to be combined into a single shear strain time history. This was accomplished by taking the square-root of the sum-of-the-squares for the two shear strain time histories. This approach is similar to reorienting the direction of the recorded time histories to find the value of maximum ground acceleration and assuming that the contribution of the minimum component is generally negligible.

The resulting shear strain time history is a series of half cycles as shown in Figure 5-4. From this time history, Equation 5.2 was used to create a continuous time history of volumetric strain. The volumetric strain determined using Equation 5.2 has two components, elastic and plastic. The elastic portion is assumed to equal zero as suggested by Byrne (1991). The change in pore pressure resulting from the plastic strain can be computed using Equation 5.3:

$$\Delta u = M\Delta\varepsilon_v^p \tag{5.3}$$

where Δu is the incremental change in pore water pressure, and M is the rebound effective stress constrained tangent modulus. Rather than developing an estimate of the rebound effective stress constrained tangent modulus (a value which would seem to decrease as the soil undergoes liquefaction, hence making its determination problematic), direct linkage between volumetric strain and the excess pore pressure ratio was made using Dobry and Ladd's (1980) relationship between shear strain, γ_{cyc}, and excess pore pressure ratio, R_u , as shown in Figure 5-5.

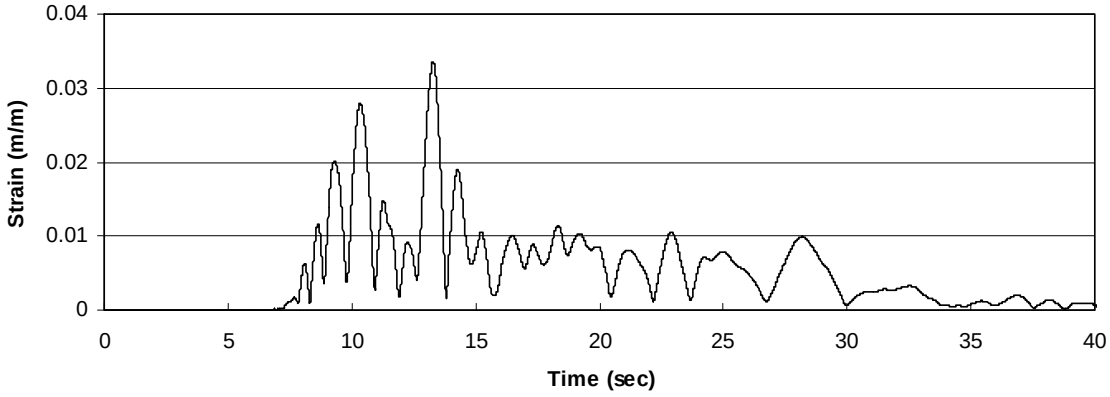

Figure 5-4: Half cycles of shear strain used to determine volumetric strain and excess pore pressure ratio

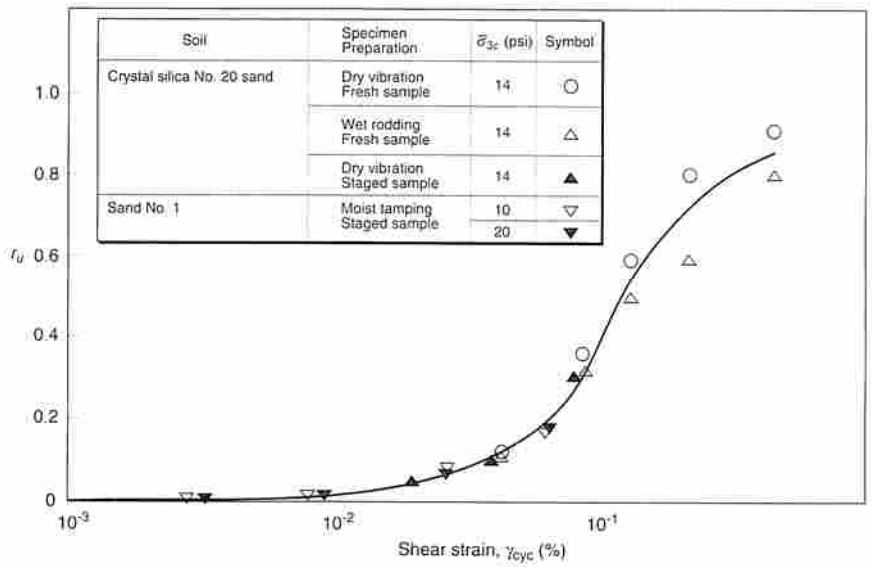

Figure 5-5: Relationship between pore pressure ratio for cyclic shear strain based on Dobry and Ladd (1980)

As shown in Figure 5-5, when the excess pore pressure ratio is expressed as a function of cyclic shear strain, the ratio is relatively independent of sample preparation methods and confining pressure, σ_{3c}. The various samples shown also represent differing relative densities, thus indicating that the relationship is generally applicable to more than one type of sand deposit. The relationship shown in Figure 5-5 is based on ten cycles of strain. Using Byrne's equation (Equation 5.2), the amount of volumetric strain corresponding to ten cycles of the shear strain shown in Figure 5-5 might be determined, thus providing a direct relationship between accumulating shear strain and the excess pore pressure ratio. However, the relationship shown in Figure 5-5 is based on triaxial compression tests (TXC). Recent work by Hazirbaba (2005) shows that the relationship between excess pore pressure and cyclic strain depends upon the type of test used to develop the relationship. Hazirbaba found the direct simple shear (DSS) test, which represents field loading conditions better than the TXC test, generates less pore water

pressure for a given cyclic shear strain. Using Hazirbaba's results, the relationship of Dobry and Ladd was modified as shown in Figure 5-6 and then used to determine the development of excess pore pressure with accumulating cycles of shear strain.

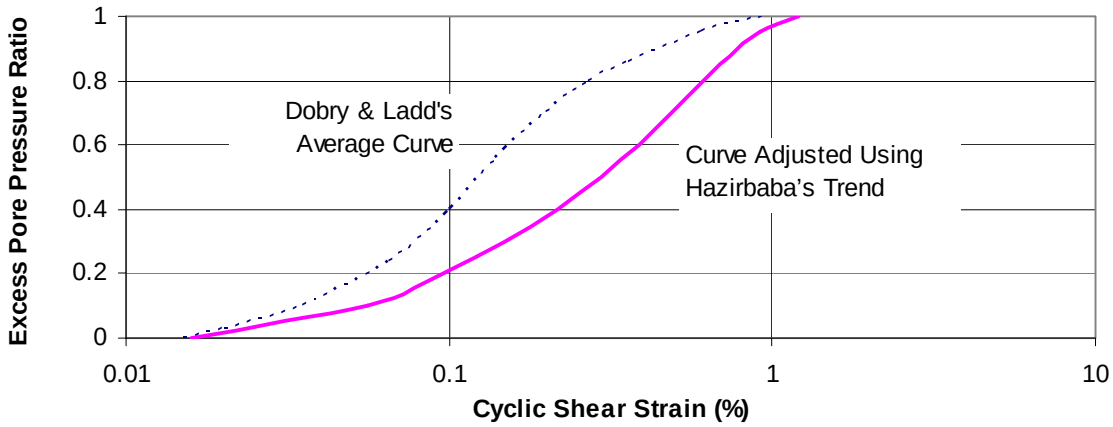

Figure 5-6: Adjusted relationship between pore pressure ratio for cyclic shear strain

The excess pore pressure ratio time history calculated for the PIDA site is shown in Figure 5-7. In Figure 5-7, the excess pore pressure ratio begins to increase rapidly at approximately 7.4 seconds and levels off at an excess pore pressure equal to approximately 0.95 (95%) at about 13 seconds. It is during the time period from 7.4 to 13 seconds that the shear modulus in Figure 4-18 and Figure 4-20 is seen to degrade more than would be expected by increasing shear strain alone. This behavior correlates with the rapid rise in pore water pressure and the onset of liquefaction.

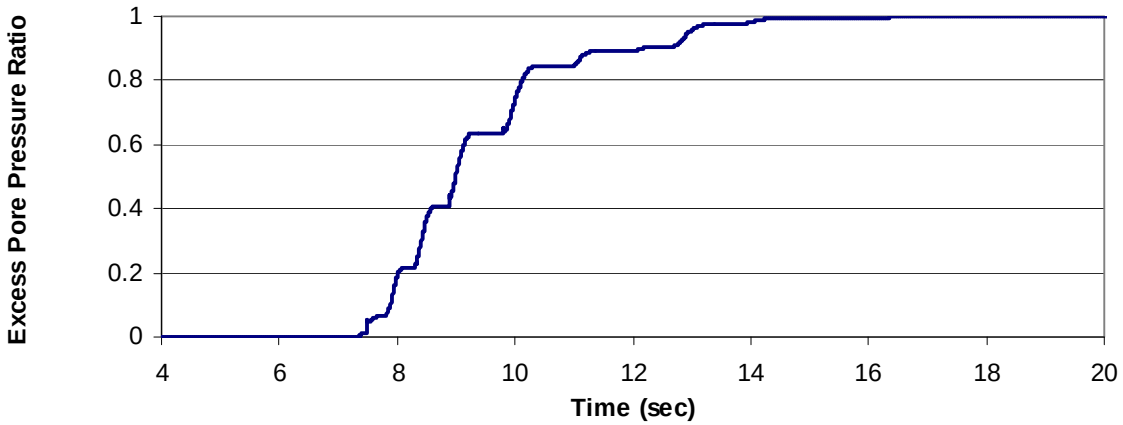

Figure 5-7: Excess pore water pressure ratio time history

As mentioned previously, measured shear strains were used to determine the excess pore water pressure ratio time history. This determination was made prior to conducting the site response analysis. Unless an iterative or coupled process is used, the shear strain cycles used to determine the excess pore water pressure ratios would not be known until the shear stresses from the previous time step had been computed. However, for the purposes of assessing the validity of the degrading backbone method, using an 'a priori' excess pore pressure ratio time history was considered acceptable. In an iterative or coupled approach, both components of the input ground motion would need to be considered together to determine a single representative strain time history. There also might be numerical convergence issues when strains are relatively large (i.e., strains plot on the flatter-sloped portions of the stress-strain curve) and the stress-strain curves themselves become flatter due to a small modulus scaling factor accompanying a high excess pore pressure ratio.

5.4 Results and Interpretation of Results

The shear stress time history for the liquefying soil layer based on the North-South (NS) component of ground motion and the degrading backbone curve method is shown in Figure 5-8. Also shown in this figure is the "actual" shear stress time history presented previously in Section 4.2. By combining the shear stresses shown in Figure 5-8 with the shear strain time history shown in Figure 5-9, actual and model-based shear stress-strain hysteretic loops were created. These plots are shown in Figure 5-10 and Figure 5-11, respectively. While the actual and model results do not match exactly, they reflect the same overall stress-strain behavior throughout the duration of the earthquake.

As shown in Figure 5-8, the model accurately predicts the trends in the actual stress time history. There is a lot more activity in the actual time history than in the modeled before the initial onset of excess pore water pressure development at about 7 seconds. Part of the reason for this is the limited ability of the algorithm to capture the higher frequencies present in the ground motion up to this point. Once excess pore water pressure develops, the model time history matches the trends of the actual time history. The largest deviance after the onset of elevated pore water pressures occurs is around 11.3 seconds. At this time, the stress given by the model is approximately half of the actual stress. It appears that the shear modulus model has softened too quickly at this juncture. After about 19 seconds, the model begins to overestimate the stress somewhat, but at this point the major accelerations have already occurred and only small reverberations remain in the time history. However, between approximately 7 to 19 seconds, the model does predict the stresses within the liquefying soil quite well.

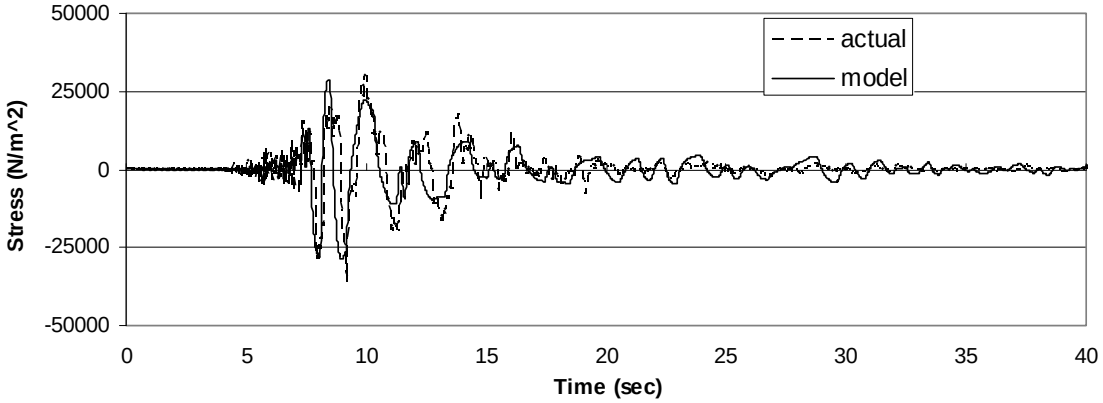

Figure 5-8: Actual and modeled shear stress time histories, NS

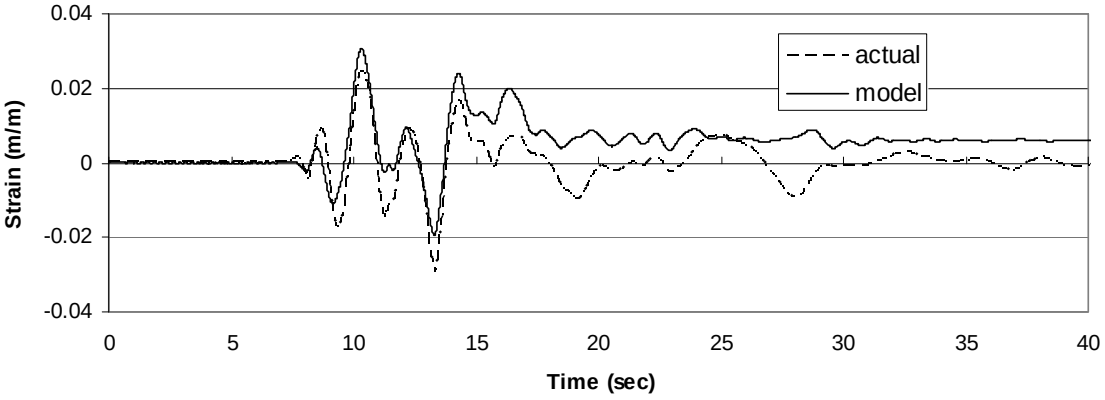

Figure 5-9: Actual and modeled shear strain time histories, NS

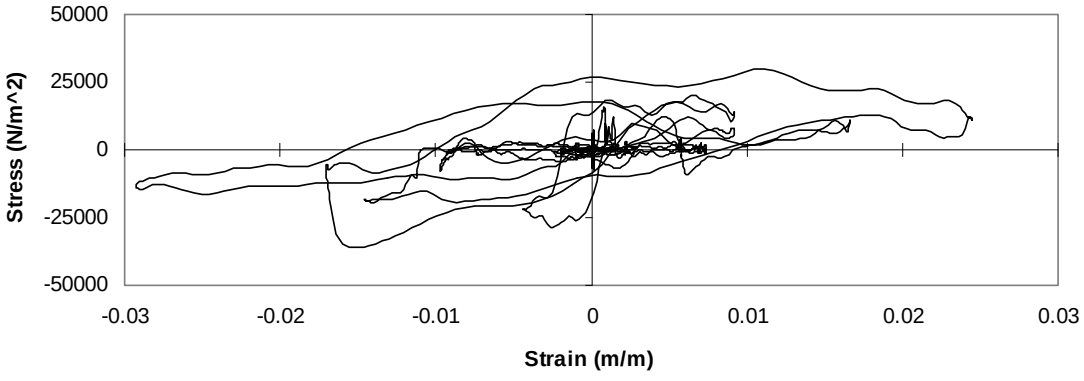

Figure 5-10: Actual stress-strain hysteretic loops, NS

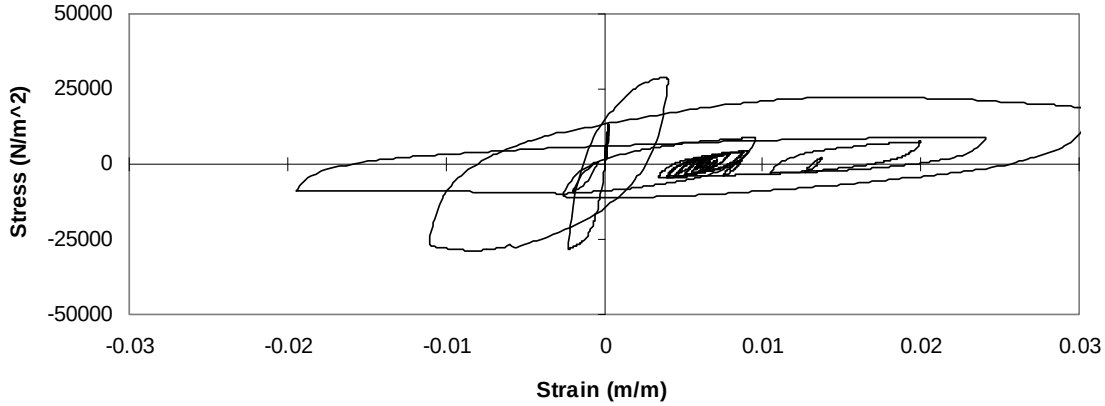

Figure 5-11: Modeled stress-strain hysteretic loops, NS

The match between the actual and modeled shear strains shown in Figure 5-9 is not as good. In general, the model-based peak strains during the period of significant ground shaking are under-estimated. After this point, the model-based strains are shifted in the positive direction, creating an artificial residual strain. This is likely a result of a underestimation of strain immediately after 12.7 sec from which the model does not recover.

In comparing the actual and model-based shear stress-strain hysteretic loops, a fair degree of consistency in the varying shear moduli can be seen, particularly after making an allowance for the offset in strain occurring around 12.7 sec. The model-based shear stress-strain loops do tend to be less rounded flatter and more uniform than the actual loops, particularly away from the endpoints. For greater clarity, individual shear stress-strain loops for four different time intervals have been isolated and enlarged and are shown in Figure 5-12 through Figure 5-15. The actual and model hysteretic loops match well nearer to the onset of excess pore water pressure generation whereas later during the motion near 12.7 sec there is the noted localized drift in the strain time history.

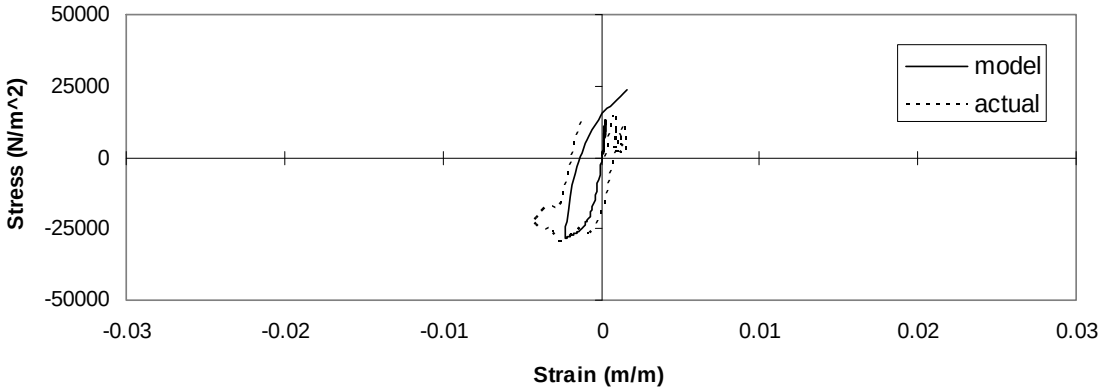

Figure 5-12: Comparison of actual and modeled stress-strain loops for 7.3 to 8.3 seconds, NS

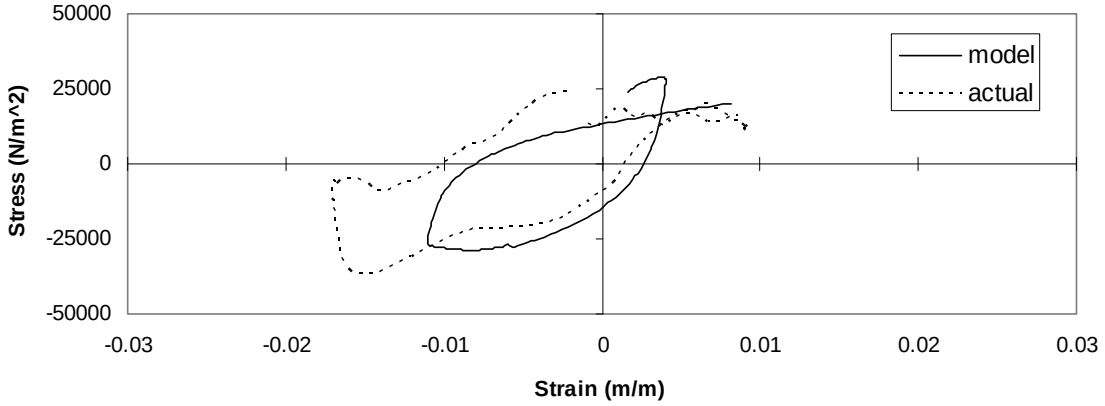

Figure 5-13: Comparison of actual and modeled stress-strain loops for 8.3 to 9.8 seconds, NS

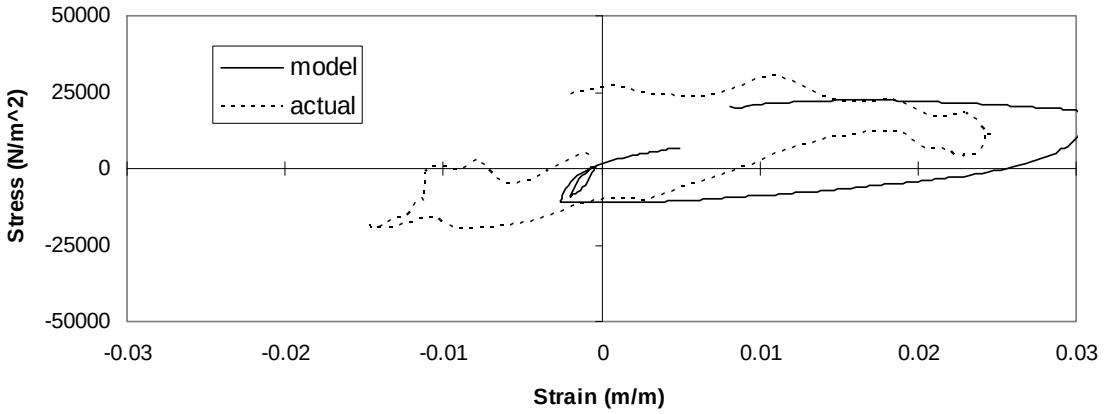

Figure 5-14: Comparison of actual and modeled stress-strain loops for 9.8 to 11.9 seconds, NS

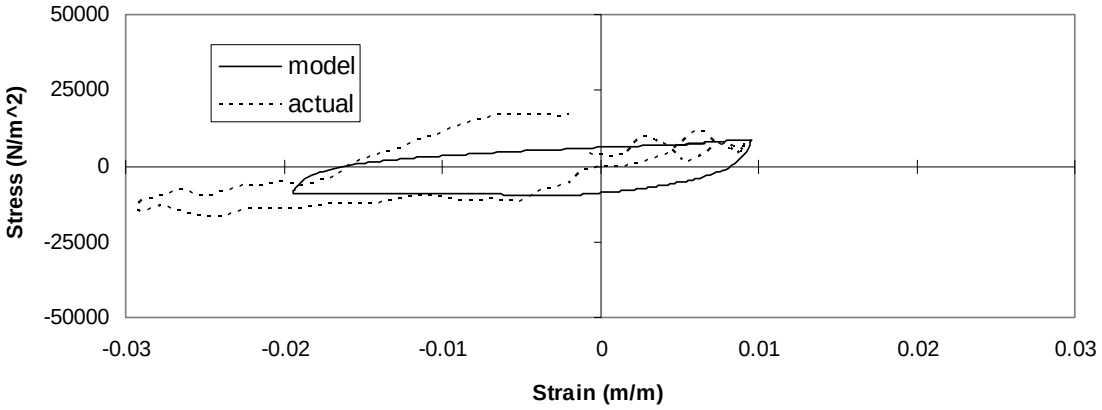

Figure 5-15: Comparison of actual and modeled stress-strain loops for 11.9 to 13.8 seconds, NS

This difference corresponds to the same juncture when shear stress was underestimated, as discussed previously. The actual and model loops still show the same general shape despite the lateral shift.

The shear stress time history for the liquefying soil layer based on the East-West (EW) component of ground motion and the degrading backbone curve method is shown in Figure 5-16. Also shown in this figure is the "actual" shear stress time history presented previously in Section 4.2. By combining the shear stresses shown in Figure 5-16 with the shear strain time history shown in Figure 5-17, actual and model-based shear stress-strain hysteretic loops were created. These plots are shown in Figure 5-18 and Figure 5-19, respectively. The agreement between the actual behavior and model results for the East-West direction are better than those observed for the North-South direction. Before and during excess pore water pressure generation, the values for the East-West direction exhibit very good agreement. During the 10 to 11 second time period when the estimated pore water pressure ratio jumps rapidly from 0.65 to 0.85, the model stress time history exhibits its largest deviance from the actual stress time history.

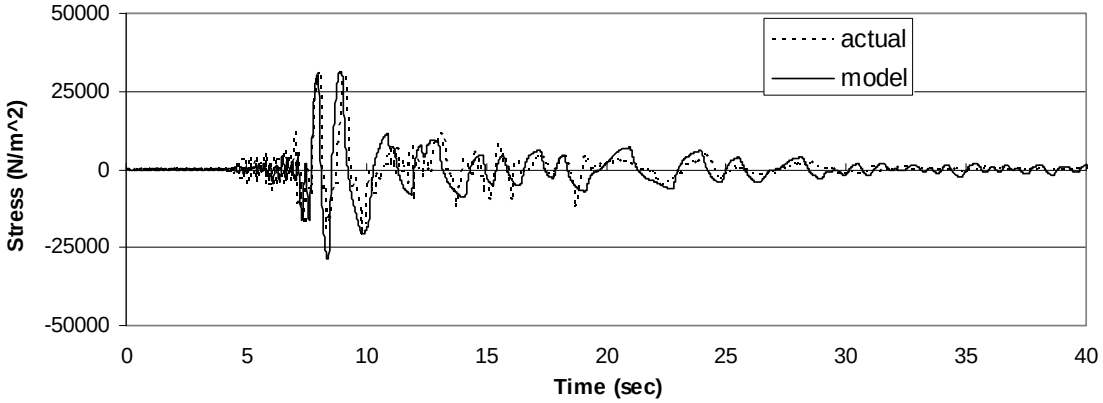

Figure 5-16: Actual and modeled shear stress time histories, EW

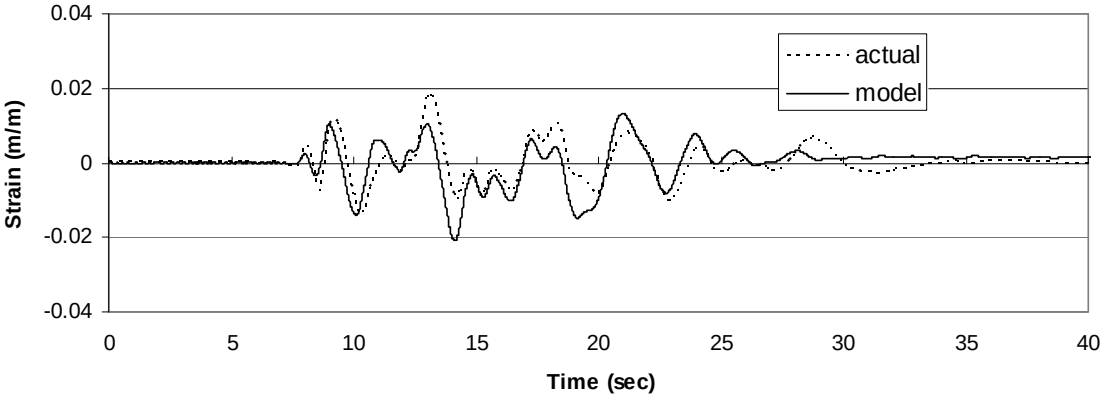

Figure 5-17: Actual and modeled shear strain time histories, EW

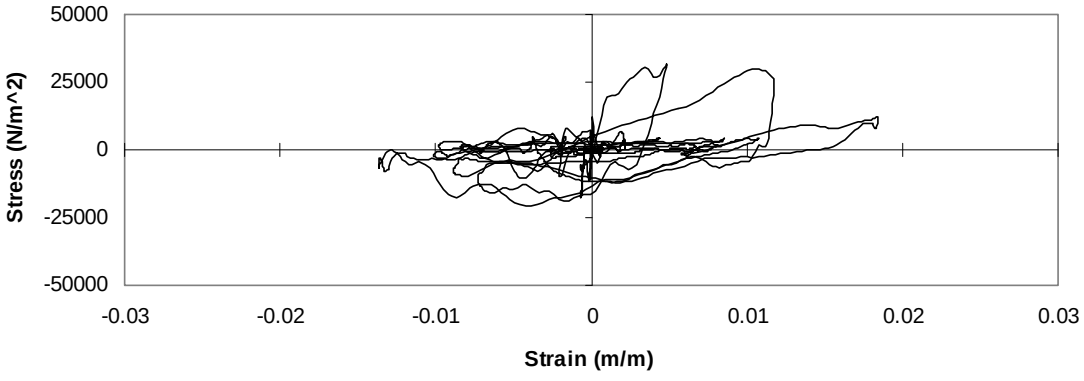

Figure 5-18: Actual stress-strain hysteretic loops, EW

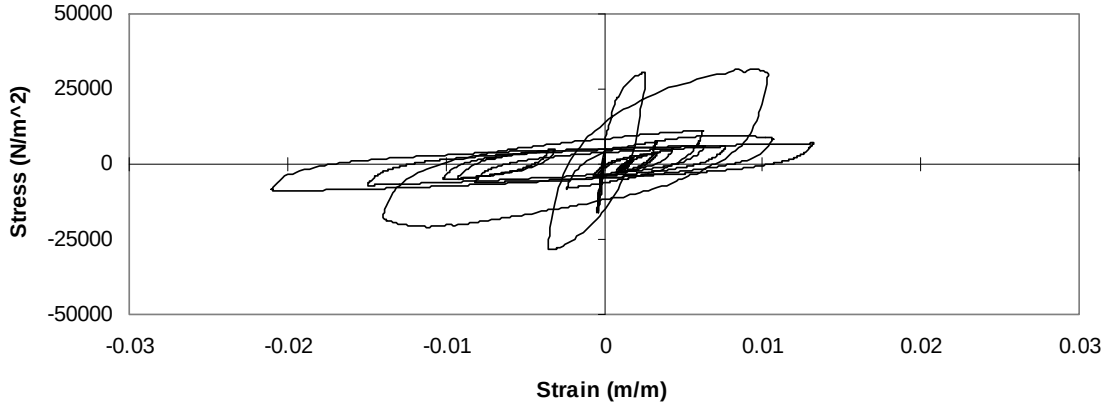

Figure 5-19: Modeled stress-strain hysteretic loops, EW

Given the differences observed in the North-South direction for this same time period, it appears that the shear modulus may be too soft in the time interval. However, even with this variance, the model-based stress and strain time histories generally match the actual time histories up through the end of the record. The offset in strain observed in the North-South direction is not present in the East-West direction, and overall the agreement in strain is better.

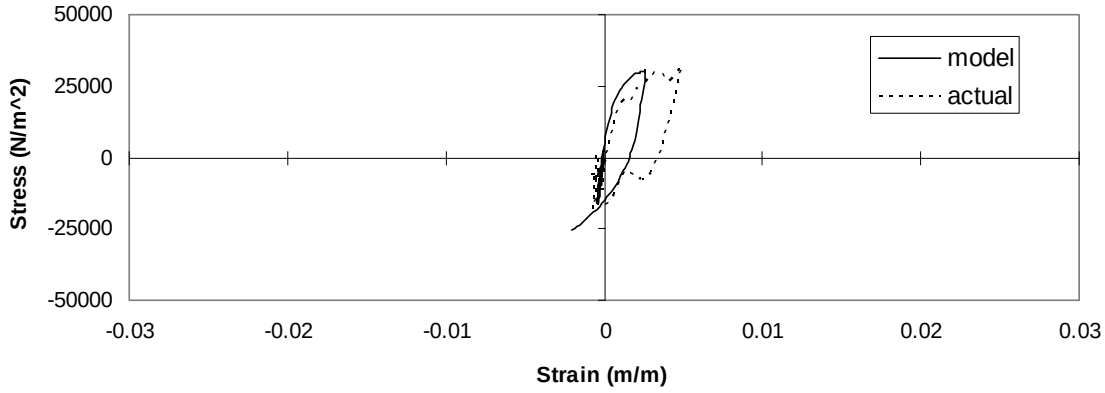

Figure 5-20: Comparison of actual and modeled stress-strain loops for 7.2 to 8.3 seconds, EW

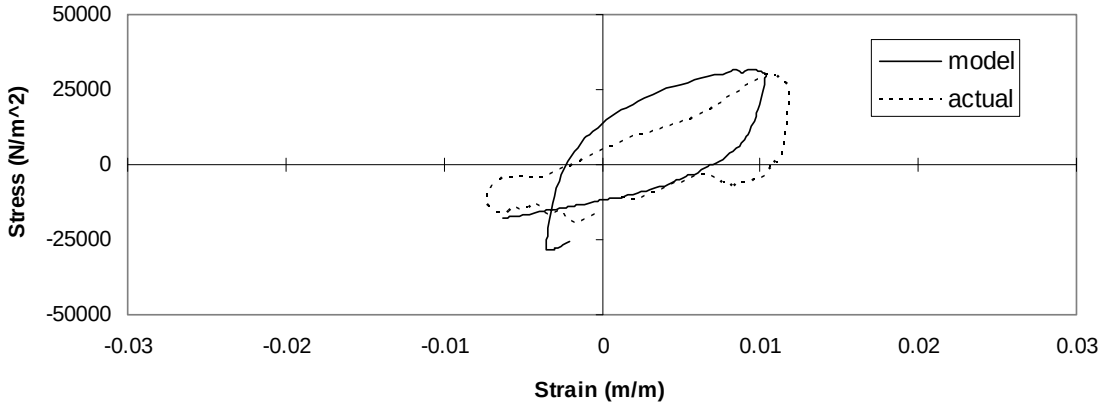

Figure 5-21: Comparison of actual and modeled stress-strain loops for 8.3 to 9.7 seconds, EW

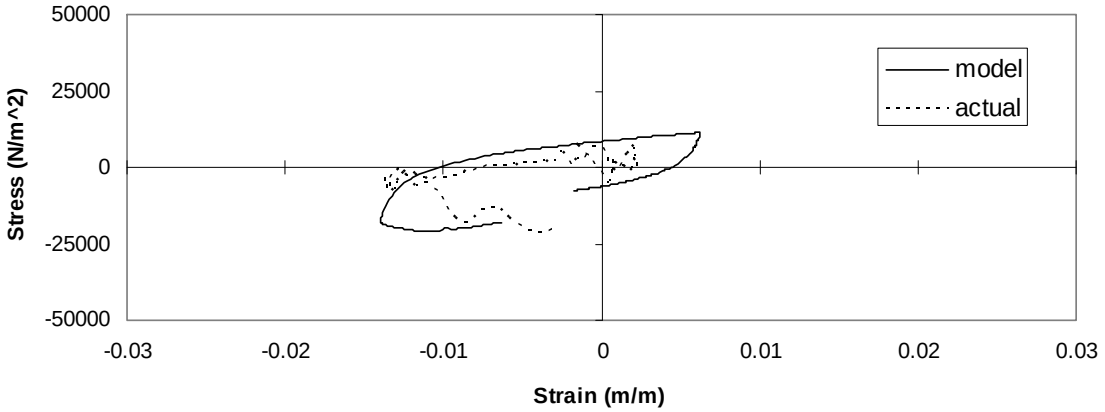

Figure 5-22: Comparison of actual and modeled stress-strain loops for 9.7 to 11.8 seconds, EW

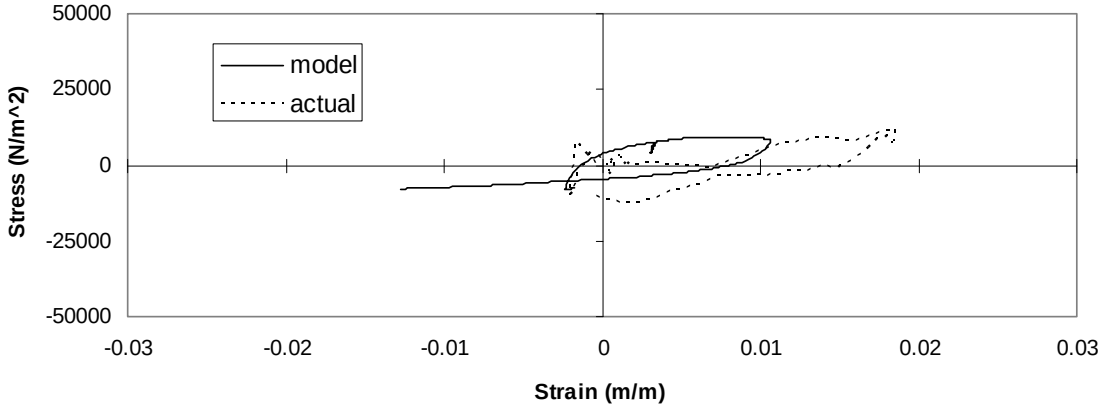

Figure 5-23: Comparison of actual and modeled stress-strain loops for 11.8 to 13.8 seconds, EW

In examining shear stress-strain hysteretic loops, the same type of shear modulus decrease is seen. In the case of the East-West component, a very good agreement exists between model and actual stresses. The actual East-West hysteretic loops are more linear than the North-South loops. For improved clarity, individual shear stress-strain loops for four different time segments have been isolated and enlarged as shown in Figure 5-20 through Figure 5-23. Even at this scale, the agreement between model and actual stress-strain loops appears to be very good.

The acceleration time history of the liquefied surface layer produced by the model is compared to the actual time histories for both the North-South and the East-West directions in Figure 5-24 and Figure 5-25. Since acceleration is directly proportionate to shear stress in Equation 4.3, the modeled and actual accelerations have the same degree of agreement as the modeled and actual shear stresses. The acceleration time histories match fairly well during the time period of greatest acceleration.

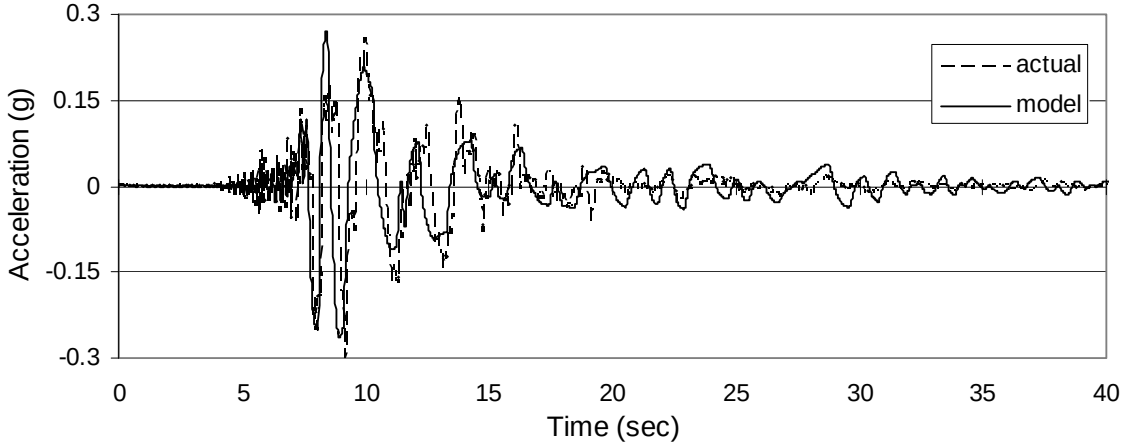

Figure 5-24: Actual and modeled acceleration time histories, NS

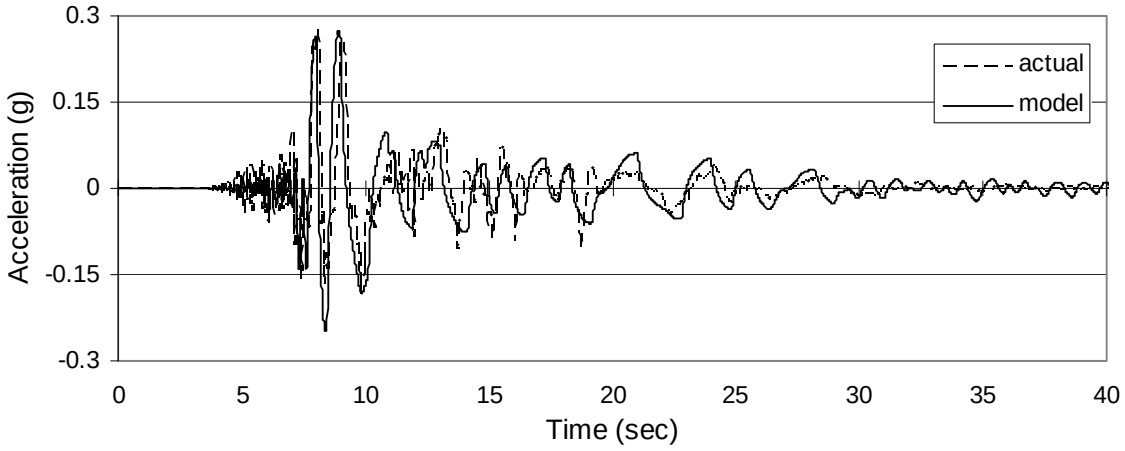

Figure 5-25: Actual and modeled acceleration time histories, EW

The acceleration response spectra produced by the degrading backbone model can also be compared to the acceleration response spectra based on the actual ground motions. The model and actual acceleration response spectra for the North-South direction are presented in Figure 5-26, while spectra for the East-West direction are presented in Figure 5-27. The model-based acceleration response spectra agree well overall with the acceleration response spectra from the actual earthquake. In the North-South direction, the predominant period of the model is somewhat less than the predominant period of the actual ground motions (compare approximately 0.96 to 1.25 seconds). However, the peak spectral accelerations are about the same. A similar shift in predominate period occurs in the East-West direction (compare approximately 0.96 to 1.15). These results result largely from a delayed degradation of shear modulus in the model at about 7 seconds. Close inspection of the strain time histories shows an under-estimation of shear strain at this juncture, indicating that the modeled soil behavior is too stiff. The model-based spectrum for the North-South direction varies between under or over predicting the spectral response while the spectrum for the East-West direction

greater than 0.6 seconds over predicts the spectra response. The largest over prediction by percentage occurs near a period of 2 seconds.

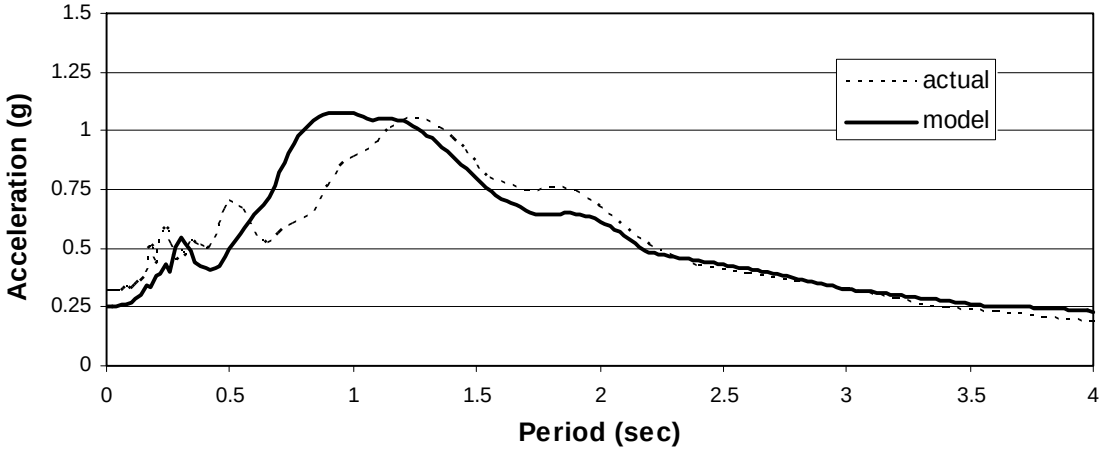

Figure 5-26: Actual and modeled acceleration response spectrum, NS surface

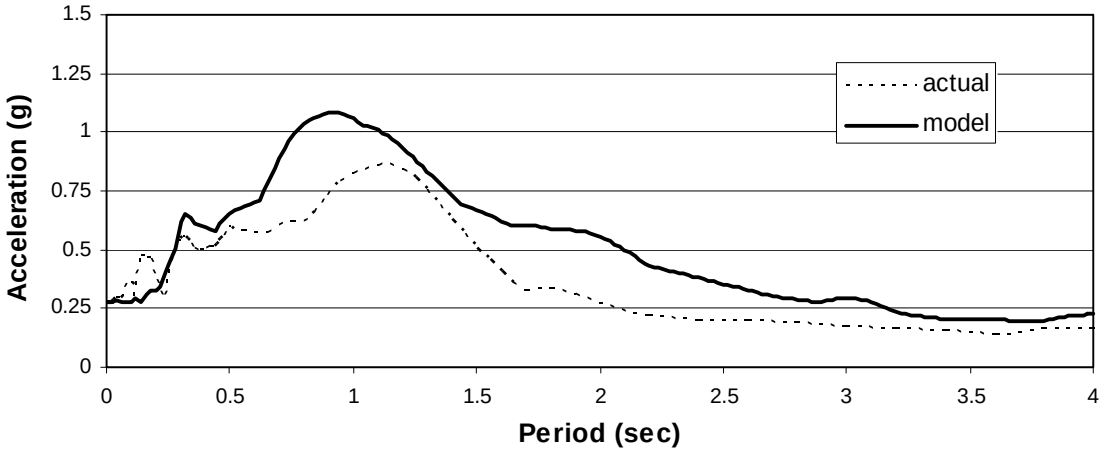

Figure 5-27: Actual and modeled acceleration response spectrum, EW surface

The displacement response spectra produced from the model have been compared to the actual displacement response spectra. The model and actual displacement response spectra for the North-South direction are presented in Figure 5-28. The same spectra for

the East-West direction are presented in Figure 5-29. The spectra in the North-South direction show a very good match, while the match in the other direction is just fair.

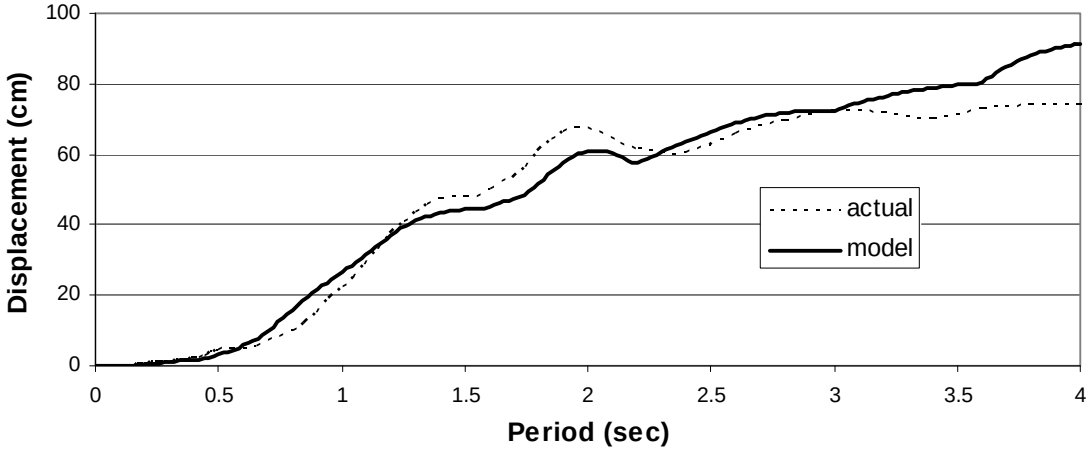

Figure 5-28: Actual and modeled displacement response spectrum, NS surface

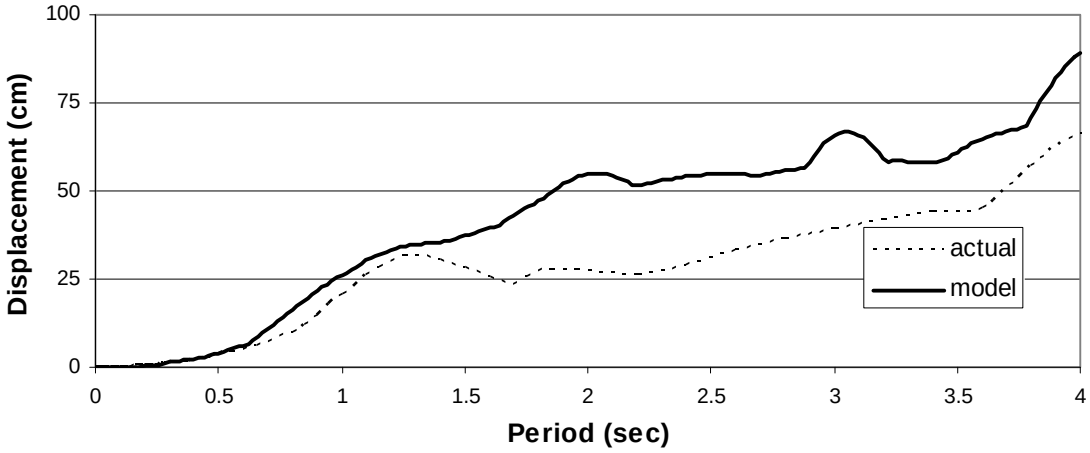

Figure 5-29: Actual and modeled displacement response spectrum, EW surface

Given the fact that the shear modulus degradation curve initially used in developing the degraded backbone curve model is Seed and Idriss' (1970) "average" sand curve and was not selected based on extensive laboratory testing, coupled with the relative simplicity of the method used to estimate the development of excess pore water

pressures, the agreement obtained between the model and actual values presented in this thesis is judged to be good. This assessment is substantiated by comparison with the response spectra that would have resulted had the non-liquefiable soil been present. As shown by Youd and Carter (2003) in Figure 3-29 and Figure 3-30, the difference between the liquefied and non-liquefied acceleration response spectra is drastically greater than the difference between the model-based and actual spectra.

6 Summary, Conclusions, and Recommendations

6.1 Summary

In this thesis, ground motions recorded by an array of downhole accelerometers on Port Island, Japan, during the 1995 Kobe Earthquake, are used to quantify the shear modulus of sand as it liquefies. An approach to modeling the degradation of shear modulus of sand as it liquefies is also presented. This approach consists of a typical shear modulus degradation curve whose shape is altered in response to the development of excess pore water pressures. This approach is called the "degrading shear modulus backbone curve" model. The hysteretic shear stress behavior of the liquefied sand is computed using a non-linear Iwan-Mroz model fit to the degrading backbone curve. The resulting shear stresses and ground accelerations computed using the model are in good agreement with actual values. The model presented in this thesis reasonably matches the actual ground response at the Port Island Downhole Array (PIDA) site.

6.2 Conclusions

Based on data from the Port Island Downhole Array (PIDA) site obtained during the 1995 Kobe Earthquake and the work presented in this thesis, the following conclusions are made:

- The shear modulus of sand decreases significantly as it liquefies, apparently decreasing in proportion to increasing excess pore water pressure.

- The process of excess pore pressure generation and liquefaction can occur relatively quickly during an earthquake; at the PIDA site during the Kobe Earthquake, the process took approximately 6 seconds.
- For an initial relative density of 40 to 50%, the shear modulus of liquefied sand is approximately 1% of its initial low-strain value; this corresponds to approximately 15% of the high-strain modulus of sand in its non-liquefied state.
- A degrading shear modulus backbone curve can reasonably model shear modulus degradation during liquefaction and the degradation of the backbone curve is a function of the excess pore water pressure ratio.
- Using a non-linear Iwan-Mroz model fit to the degrading backbone curve, the complete hysteretic shear stress-behavior of the liquefied sand can be computed.
- The shear stresses and back-calculated ground accelerations obtained using the degrading shear modulus backbone method reasonably match those occurring at the Port Island Downhole Array (PIDA) site during the 1995 Kobe Earthquake.

6.3 Recommendations

Based on the work presented in this thesis, the following recommendations are offered:

- The degrading shear modulus backbone method can be used when conducting ground response analyses at sites with liquefiable soils (subject to the remaining recommendations).

- The degrading shear modulus backbone method should be refined and validated for soils of different relative densities and using different site conditions.
- A more robust and coupled method for determining the development of excess pore water pressures should be developed for incorporation into the degrading shear modulus backbone method.

7 References

Bardet, J.P., and Tobita, T. (2001). NERA: A Computer Program for Nonlinear Earthquake site Response Analysis of Layered Soil Deposits, University of Southern California, Department of Civil Engineering.

Bardet, J.P., Oka, F., Sugito, M., and Yashima, A. (1995). The Great Hanshin Earthquake Disaster: Preliminary Investigation Report, University of Southern California, Los Angeles, California.

Byrne, P.M. (1991). "A cyclic shear-volume coupling and pore pressure model for sand." Proceedings: Second International Conference on Recent Advances in Geotechnical Earthquake Engineering and Soil Dynamics, March 11-15, 1991, St. Louis, Missouri, Vol. 1. 47-55.

Dobry, R., and Ladd, R.S. (1980). "Discussion to 'Soil liquefaction and cyclic mobility evaluation for level ground during earthquakes' by H.B. Seed and 'Liquefaction potential: science versus practice' by Ralph Peck." *Journal of the Geotechnical Engineering Division*, American Society of Civil Engineers, 106(GT6), 720-724.

EduPro Civil Systems, Inc. (1998). "ProShake User's Manual." Version 1.1, Redmond Washington.

Elgamal, A.W., Zeghal, M., and Parra, E. (1996). "Liquefaction of reclaimed island in Kobe, Japan." *Journal of Geotechnical Engineering*, American Society of Civil Engineers, 122(1), 39-49.

Hazirbaba, K. (2005). "Pore pressure generation characteristics of sands and silty sands: a strain approach." *PhD Dissertation.* University of Texas at Austin, Austin, Texas.

Ishihara, K., Cubrinovski, M., and Nonaka, T. (1998). "Characterization of undrained behavior of soils in the reclaimed area of Kobe." *Special Issue of Soils and Foundations [on Geotechnical Aspects of the January 17, 1995 Hyogoken-Nambu Earthquake, No 2]*, 33-46.

Jelinek, K. (2000). "In-Situ Measurements of Shear Wave Velocities After Blast Induced Soil Liquefaction" MS Thesis, Civil and Environmental Engineering Dept. Utah State University.

Kramer, S. L. (1996). *Geotechnical Earthquake Engineering.* Prentice Hall., New Jersey.

Martin, P.P., and Seed, H.B. (1979). "Simplified procedure for effective stress analysis of ground response." *Journal of the Geotechnical Engineering Division*, American Society of Civil Engineers, 105(GT6), 739-758.

Nakakita, Y., and Watanabe, Y. (1981). "Soil stabilization by preloading in Kobe Port Island." Proc., 9th Int. Conf. on Soil Mech. and Found. Engrg., Japanese Soc. of Soil Mech. and Found. Engrg., Tokyo, Japan, 611-622.

Rollins, K.M., Evans, M.D., Diehl, N.B., and Daily, W.D. III. (1998). "Shear Modulus and Damping Relationships for Gravels." *Journal of Geotechnical and Geoenvironmental Engineering*, American Society of Civil Engineers, 124(5), 396-405.

Rollins, K. M, Lane, J.D., Nicholson, P.G., Rollins, R.E. (2004). "Liquefaction hazard assessment using controlled-blasting techniques." Procs. 11th Intl. Conf. on Soil Dynamics and Earthquake Engineering, Stallion Press, Vol. 2, 630-637.

Schnabel, P. B., Lysmer, J., and Seed, H. B. (1972). "Shake" Earthquake Engineering Research Center, Report No. EERC 72-12, December 1972.

Seed, H.B., and Idriss, I.M. (1970). "Soil moduli and damping factors for dynamic response analysis." EERC Rep. 70-10, Univ. of California, Berkeley, Calif.

Seed, H.B., Wong, R.T., Idriss, I.M., and Tokimatsu, K. (1986). "Moduli and damping factors for dynamic analyses of cohesionless soils." *Journal of Geotechnical Engineering*, American Society of Civil Engineers, 112(11), 1016-1032.

University of Washington (UofW) Website. (2000). http://www.ce.washington.edu/~liquefaction/html/main.html

United States Geological Survey (USGS) Website. (2006). http://earthquake.usgs.gov/regional/world/events/1995_01_16.php

Youd, T.L., and Carter, B.L. (2003a). "Influence of Soil Softening and Liquefaction on Response Spectra for Bridge Design" Utah Department of Transportation Research and Development Division Report No. UT-03.07, March 2003.

Youd, T.L., and Carter, B.L. (2003b). "Influence of Soil Softening and Liquefaction on Spectral Acceleration" *Journal of Geotechnical and Geoenvironmental Engineering*, American Society of Civil Engineers, 131(7), 811-825.